Article:

Malatesta, L.C. orcid.org/0000-0003-0983-715X, Avouac, J.-P., Brown, N.D. et al. (9 more authors) (2018) Lag and mixing during sediment transfer across the Tian Shan piedmont caused by climate-driven aggradation-incision cycles. Basin Research, 30 (4). pp. 613-635. ISSN 0950-091X

https://doi.org/10.1111/bre.12267

Lag and mixing during sediment transfer across the Tian Shan piedmont caused by climate-driven aggradation-incision cycles
Supplementary files

Luca C. Malatesta[1], Jean-Philippe Avouac[1], Nathan Brown[2], Sebastian F. M. Breitenbach[3], Jiawei Pan[4], Marie-Luce Chevalier[4], Edward Rhodes[5],[2], Dimitri Saint-Carlier[6], Wenjing Zhang[4], Julien Charreau[6], Jérôme Lavé[6], Pierre-Henri Blard[6]

---

1 Introduction

Details of the sampling and analytical methods are listed in the supplementary file. Most of it is a description of the 20 post-IR IRSL samples collected by the Caltech-CAGS field mission to the Chinese Tian Shan in June and July 2013 and analysed in the UCLA luminescence laboratory. The detailed method for cosmogenic nuclide analysis is in Section 3. Information about the samples is listed in Section 4. Each sample location is described in Figures 3 to 26 with a wide view of the outcrop and a close-up view of the deposits. The photos are embedded at high-resolution in the pdf. The analytical results are illustrated with a sensitivity plot and a radial plot of single-grain equivalent dose D_e values. The UCLA lab number is indicated in brackets after the field number. The final Figure 27 shows the details of the cosmogenic profile samples collected by the 2012 CRPG Nancy mission on terrace T18 of the Anjihai River.

2 Method for luminescence dating

2.1 Sample preparation, instrumentation, and measurement protocol

K-feldspar grains of 175-200 μm were isolated from the sedimentary samples under dim amber LED light conditions. Subsamples were wet-sieved, treated with 3% HCl, separated by density with lithium metatungstate (ρ <2.565 g/cm^3; Rhodes, 2015), and treated with 10% HF for 10 minutes to remove the outer layer from the grains.

Luminescence measurements were carried out using a TL-DA-20 Risø automated reader equipped with a single-grain IR laser (830 nm, at 90% of 150 mW) and a ^{90}Sr/^{90}Y beta source. Measurements of scatter in D_e values for Risø calibration quartz suggest that source inhomogeneity causes 11% overdispersion. Emissions were detected through a Schott BG3-BG39 filter combination. Samples were mounted on aluminium single-grain discs with 100 holes.

The U and Th concentrations were measured with inductively-coupled plasma mass spectrometry (ICP-MS), and the K concentration (Table 2) was measured using inductively-coupled plasma

[1]Division of Geological and Planetary Sciences, California Institute of Technology, Pasadena, CA 91125, USA
[2]Department of Earth, Planetary, and Space Sciences, University of California Los Angeles, CA 90095, CA
[3]Institute of Geology, Mineralogy & Geophysics, Ruhr-Universität Bochum, 44780 Bochum, Germany
[4]Institute of Geology, Chinese Academy of Geological Sciences, Beijing 100037, China
[5]Department of Geography, The University of Sheffield, S10 2TN Sheffield, UK
[6]Centre de Recherches Pétrographiques et Géochimiques, Vandoeuvre les Nancy, 54500 France

optical emission spectrometry (ICP-OES). These values were used to calculate the total beta dose-rate contribution using the conversion factors of Adamiec and Aitken (1998). A value of 12.5 ± 0.12 wt. % K content was used in calculating the internal dose rate (Huntley and Baril, 1997). Sediment samples were collected within each sample hole for water content measurement, and cosmic dose-rates were estimated following Prescott and Hutton (1994).

A post-IR IRSL single-grain protocol (Buylaert et al., 2009) was used to measure equivalent dose (D_e) values. Individual grains were stimulated first at 50 °C for 3 s, and then at 225 °C for 3 s to measure the more stable post-IR IRSL signal. Preheating at 250 °C for 60 s was used before natural and regenerative measurements, as well as a stimulation with the IR diodes at 290 °C for 40 s at the end of each single-aliquot regenerative-dose (SAR) cycle Wintle and Murray (2006).

2.2 Fading correction

Faded and unfaded ages of the samples are listed in Table 2. The stimulation temperature of 225 °C for the post-IR IRSL measurement was chosen to minimise athermal fading while maximizing the solar-bleaching rate (Li and Li, 2011; Kars et al., 2014). Nevertheless, post-IR IRSL signals exhibit a range of fading values (Buylaert et al., 2009). To assess the stability of the measured signal at room temperature, we measured the sensitivity-corrected luminescence following a beta dose of 70.7 Gy, a preheat of 250 °C for 60 s and a pause ranging from 3270 s to 1.02 $\times 10^6$ s (Huntley and Lamothe, 2001). These measurements were performed for two aliquots each of samples J0654, J0656, J0658, and J0661. It has been shown that single aliquot fading measurements for density-separated K-feldspar sediments correspond to the fading values derived from the brightest individual grains of a population (Brown et al., 2015).

The measured g-values for these samples were 3.60 ± 0.69, 4.63 ± 0.94, 4.34 ± 0.70, and 4.95 ± 0.75, giving a weighted mean value of 4.32 ± 0.38 % signal loss per decade with a time constant of 3349 s (Aitken, 1985, Appendix F). These values are abnormally high for a post-IR IRSL protocol measured in the blue wavelength (e.g., Thomsen et al., 2008), but also notably uniform. We applied this fading correction to the young samples using the 'Luminescence' package within **R** (Kreutzer et al., 2012).

For some of the older samples, the equivalent dose was beyond the linear portion of the dose-response curve, rendering the g-value correction of Huntley and Lamothe (2001) inappropriate. In these cases, we followed the approach developed by Lamothe et al. (2003). A single, unfaded dose-response curve for each sample was constructed using the approach of Kars et al. (2008); the dimensionless recombination center density (ρ'; Huntley, 2006) was estimated from laboratory fading measurements as 2.98 ± 0.38 $\times 10^{-7}$. The summed luminescence intensities of each single-grain disc were used for the measured dose-response curves. The unfaded curve was then faded to its natural level using the same g-value used for the young samples (equation 6 of Lamothe et al., 2003) and the corrected equivalent dose was calculated by mapping the natural intensity to the approximated natural dose-response curve.

For Type C samples, two routines were used to determine ages: the Minimum Age model with three variables (MAM-3, Galbraith et al., 1999) and the DIscrete Minimum Model (DMM, Fuchs and Lang, 2001; Rhodes, 2015). Both methods compare well with 1σ overlap in most cases (Figure 1).

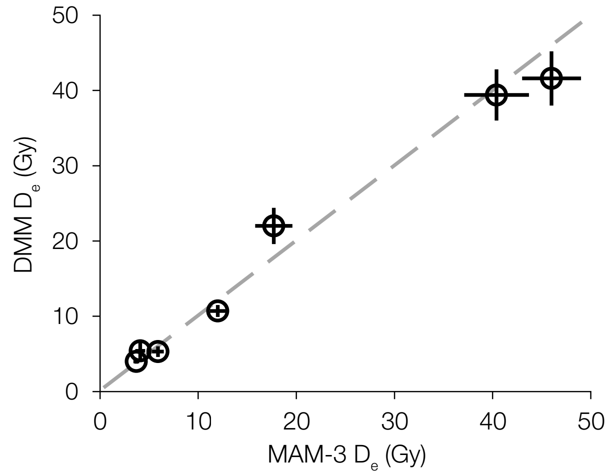

Figure 1: Results obtained using the Discrete Minimum Model (DMM; as described within the text, assuming an overdispersion of 25%) are compared against the Minimum Age Model with 3 variables (MAM-3). Note correspondence over a wide range of equivalent dose values.

Table 1: Post-IR IRSL protocol used for luminescence dating in this study. This single-aliquot regenerative cycle is repeated for the natural dose and all subsequent laboratory doses.

Step	Treatment	Description
1	Irradiation for t s	Natural dose (i.e., do nothing) for first cycle, laboratory dose for subsequent cycles
2	Heat to 250°C for 60 s	Preheat
3	IR laser stimulation at 50°C for 3 s per grain	IRSL
4	IR laser stimulation at 50°C for 3 s per grain	post-IR IRSL, Lx
5	Irradiation for t s	Test dose (same dose every cycle)
6	Heat to 250°C for 60 s	Preheat
7	IR laser stimulation at 50°C for 3 s per grain	Test dose IRSL
8	IR laser stimulation at 50°C for 3 s per grain	Test dose post-IR IRSL, Tx
9	IR diode stimulation at 290°C for 40 s	Hot bleach to empty all traps

Table 2: Detailed results of post-IR IRSL luminescence dating. 'Depth' indicates the position of the sample below the surface. The unfaded age is the final calculated age for each sample. The river acronyms are KTN (Kuitun), AJH (Anjihai), and MNS (Manas). The distribution types are described in Section 4.1.2 of the main article.

Field code	**Lab code**	**% K**	**Th (ppm)**	**U (ppm)**	**Depth (m)**	**Total dose rate (Gy/ka)**	**Equivalent dose (Gy)**	**Dist. type**	**Faded age (ka)**	**Unfaded age (ka)**
TS13_37	J0645	2.4 ± 0.1	10.6±0.5	2.6±0.13	0.75	4.324±0.206	5.4±1.1	C	1.2±0.3	1.7±0.4
TS13_36	J0646	2.4 ± 0.1	10.3±0.5	2.85±0.14	3.0	4.398±0.212	9.7±0.8	B	2.2±0.2	3.3±0.3
TS13_45	J0647	2.4 ± 0.1	8.5±0.4	2.28±0.11	0.50	4.266±0.211	22±2.4	C	5.2±0.6	7.7±1.0
TS13_86	J0648	2.1 ± 0.1	8.6±0.4	2.61±0.13	3.0	3.897±0.184	22.1±1.3	B	5.7±0.4	8.4±0.7
TS13_11	J0650	2.3 ± 0.1	10±0.5	3.63±0.18	3.0	4.386±0.205	39.4±3.4	C	9.4±1.0	13.4±1.6
TS13_06	J0651	2.1 ± 0.1	9±0.5	2.67±0.13	1.32	4.109±0.193	41.6±3.6	C	9±0.9	15.1±1.7
TS13_01	J0652	2.2 ± 0.1	9.8±0.5	2.67±0.13	38.2	3.904±0.191	276.3±16.0	A	70.8±5.6	116.8±8.1
TS13_03	J0653	2.4 ± 0.1	9.6±0.5	2.65±0.13	7.5	4.242±0.210	51.4±6.1	B	12.1±1.6	18.3±2.6
TS13_12	J0654	2.4 ± 0.1	8.6±0.4	2.32±0.12	15	4.105±0.209	433.7±28.7	B	105.7±9.1	181±13.0
TS13_08	J0655	2.2 ± 0.1	10.1±0.5	2.73±0.14	100	3.956±0.194	124.8±17.5	A	31.3±1.7	48.9±3.6
TS13_07	J0656	2.6 ± 0.1	8.7±0.4	2.29±0.11	100	4.324±0.228	518.3±59.9	B	119.9±15.4	193.4±28.0
TS13_10	J0657	2.3 ± 0.1	4.8±0.2	1.37±0.07	200	3.479±0.191	846.7±83.2	B	243.4±27.8	396.5±36.7
TS13_09	J0658	2.5 ± 0.1	7.6±0.4	1.92±0.10	200	3.995±0.213	923.6±55.7	B	231.2±19.2	316.9±24.3
TS13_02	J0659	2.5 ± 0.1	8.4±0.4	2.11±0.11	200	4.160±0.219	839.2±134.9	B	201.8±34.4	286.1±40.9
TS13_19	J0661	2.4 ± 0.1	11.1±0.6	4.05±0.20	1.0	4.346±0.197	10.7±0.8	C	2.5±0.2	3.6±0.3
TS13_35	J0662	1.7 ± 0.1	7.5±0.4	1.91±0.10	10	2.177±0.094	53±8.0	A	24.3±3.9	37.4±6.4
TS13_14	J0663	2.3 ± 0.1	10±0.5	2.53±0.13	0.80	4.246±0.202	5.3±0.7	C	1.2±0.2	1.7±0.3
TS13_34	J0664	1.5 ± 0.1	5.7±0.3	1.68±0.08	4.0	3.017±0.137	489.2±58.9	B	162.2±21.1	236.1±26.3
TS13_32	J0665	2.2 ± 0.1	10.4±0.5	3.55±0.18	10	4.087±0.190	319.3±14.4	B	78.1±5.3	111±7.0
TS13_30	J0668	1.8 ± 0.1	5.2±0.3	3.51±0.18	4.0	3.642±0.168	188±15.0	B	51.6±4.9	81.3±9.0
TS13_33	J0669	2.2 ± 0.1	9.5±0.5	3.57±0.18	5.0	4.039±0.187	578.7±62.1	B	143.3±17.0	198.1±20.5

3 Method for cosmogenic profile

3.1 Methods and parameters

Details of the sampling location and analytical results of sample TS12_ANJ_T1B are presented in Figure 27. We infer the age of surface abandonment from the depth distribution of cosmogenic isotope concentration (Dunai, 2010; Gosse and Phillips, 2001). To better account for the potential deposit of loess and/or soil after terrace abandonment, we followed the approach of Braucher et al. (2000) and Guralnik et al. (2011) and modified the general formulation of Lal (1991) as follow:

$$C(z,B) = -\overline{C_0}\mathrm{e}^{\lambda x/B} + \sum_{i=n,m_1,m_2} \frac{P_i}{\frac{\rho B}{\Delta_i}+\lambda}\,\mathrm{e}^{-\rho z/\Delta_i}\left(1-\mathrm{e}^{\frac{\lambda}{B}+\frac{\rho}{\Delta_i}z}\right) \qquad (1)$$

Where B is a ‘negative’ denudation rate (Braucher et al., 2000) which represents the accumulation rate or burial rate since terrace abandon; t represents the time since initial exposure of the surface (in this case, the abandonment of the terrace surface); C_0 is the average cosmogenic inheritance (in atoms/g); λ is the decay constant of ^{10}Be equal to $\ln(2)/T_{1/2}$ where $T_{1/2}$ is the half-life of 1.387 Ma (Chmeleff et al., 2010; Korschinek et al., 2010); n, m_1, and m_2 refer to the neutrons, fast muons and slow muons, respectively; Δ is the respective attenuation length of neutrons, slow muons and fast muons (∼160, ∼1500, ∼4320 g/cm^2 respectively) from Braucher et al. (2011) ; P is the respective local production rates (at g^{-1} yr^{-1}) for the neutrons, slow muons and fast muons; and ρ is the soil density (g/cm^3). This new formulation assumes that the few tens of centimeters of loess covering the terraces accumulated at a constant rate since the terraces abandonment. The exposure time of each sample is therefore dependent of its depth ($t = z/B$).

The local ^{10}Be production rates, P, for neutrons, fast muons and slow muons were scaled for local latitude and altitude according to Stone (2000) and the local atmospheric pressures were extracted from the ERA40 dataset (Uppala et al., 2005). In this study, we used the SLHL (see level high latitude) production rate of 3.9 ± 0.1 at g^{-1} yr^{-1} that was compiled by Balco et al. (2009) and revised by Braucher et al. (2011) to include the slow and fast muons contribution. The slow and fast muonic production rates (0.01 and 0.034 at g^{-1} yr^{-1} respectively) were derived from Braucher et al. (2011). Alluvium density was estimated by analyzing pictures of the outcrop in order to determine first the relative proportions of grains larger than medium gravel ($\varnothing > 1-2$ cm) and of sand-sized to medium gravel-sized grains. Bulk density was calculated by attributing densities of 2.7 ± 0.1 g/cm^3 to coarser grains and 1.9 ± 0.1 g/cm^3 to finer grains (Hancock et al., 1999).

3.2 Sample treatment

Quartz separation and isolation of pure beryllium oxide (BeO) was performed at CRPG (Nancy, France). Samples were first crushed and sieved. The 200-800 µm fraction was then processed by magnetic separation and the non-magnetic fraction was dissolved in a mixture of H_2SiF_6 and HCl. Quartz was then purified in three successive HF baths to remove atmospheric ^{10}Be from the quartz surfaces (Brown et al., 1991; Kohl and Nishiizumi, 1992). Next, the purified quartz was completely dissolved in HF after addition of 200 µl of an in-house 2.020 10^{-3} g/g ^{9}Be carrier solution. Purified BeO samples were obtained after subsequent purification by anion exchange, cation exchange and alkaline precipitation. The ^{10}Be/^{9}Be ratios of the BeO samples were measured at the ASTER (Accelerator for Earth Sciences, Environment and Risks) national AMS (Accelerator Mass Spectrometer) facility, located at CEREGE in Aix en Provence, France. These concentrations

Table 3: Sample data set and cosmogenic results

Sample name	**Depth (m)**	**Sampling thickness (cm)**	**Pure Qz weight (g)**	^{10}**Be**/^{9}**Be** 10^{-14}	^{10}**Be counts**	[^{10}**Be**] 10^4 **(at/g)**	**error** 10^4 **(at/g)**
TS12_ANJ_T1B_P0a	0	5	10	3.7	476	9.59	0.5
TS12_ANJ_T1B_P0d	0	5	9.7	3.8	381	10.11	0.61
TS12_ANJ_T1B_P0e	0	5	25	8.9	1145	9.58	0.33
TS12_ANJ_T1B_P1	-0.3	5	4.2	2.5	248	14.84	1.09
TS12_ANJ_T1B_P2	-0.75	5	2.6	1.3	155	12.29	1.27
TS12_ANJ_T1B_P3	-1.1	5	5.9	2.5	204	10.77	0.85
TS12_ANJ_T1B_P4	-2.5	5	2.2	1.1	113	11.42	1.43

are normalized to the ^{10}Be/^{9}Be SRM 4325 NIST reference material using an assigned value of $2.79 \pm 0.03 \cdot 10^{-11}$ (Nishiizumi et al., 2007). This standardization is equivalent to 07KNSTD within rounding error. The mean ^{10}Be/^{9}Be ratio of 22 chemical blank samples is $1.7 \pm 0.7 \cdot 10^{-15}$. Blank corrections represent between 0.1% and 8% of the samples (average of 1.6%).

4 Sample locations and results

Grain size was surveyed at eight locations along the Kuitun River (Figure 2). The intermediate axes of >100 grains was surveyed on the surface of alluvial bars next to the active river channel in six locations along the Kuitun River (sampling sites I-VI) and on the dry bed of the small tributary Swallows' Canyon (sampling sites VII and VIII). The location of the sampling sites can be found in Figures 4 and 7 of the main article. Picking was done in an area of roughly 20 by 20 meters where the surveyors would walk at random and, at each step, pick the the sediment grain that their finger would first hit when reaching for the ground without looking (Wolman, 1954).

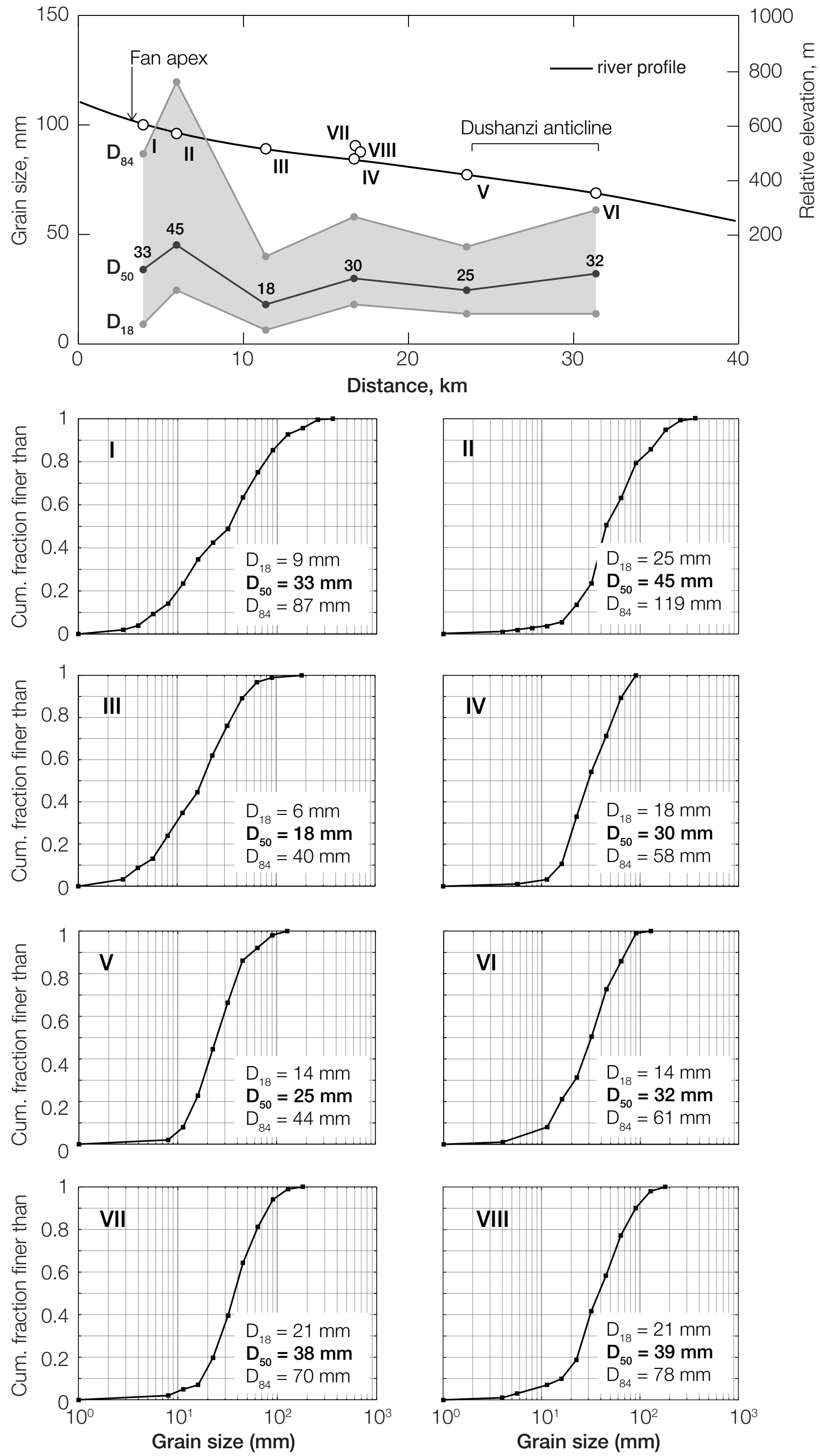

Figure 2: Grain size survey of the Kuitun River. Top: along stream evolution of the grain sizes on active banks of the Kuitun River. Bottom: cumulative fractions of grain sizes for each survey. See Figures 4 and 7 of the main article for location.

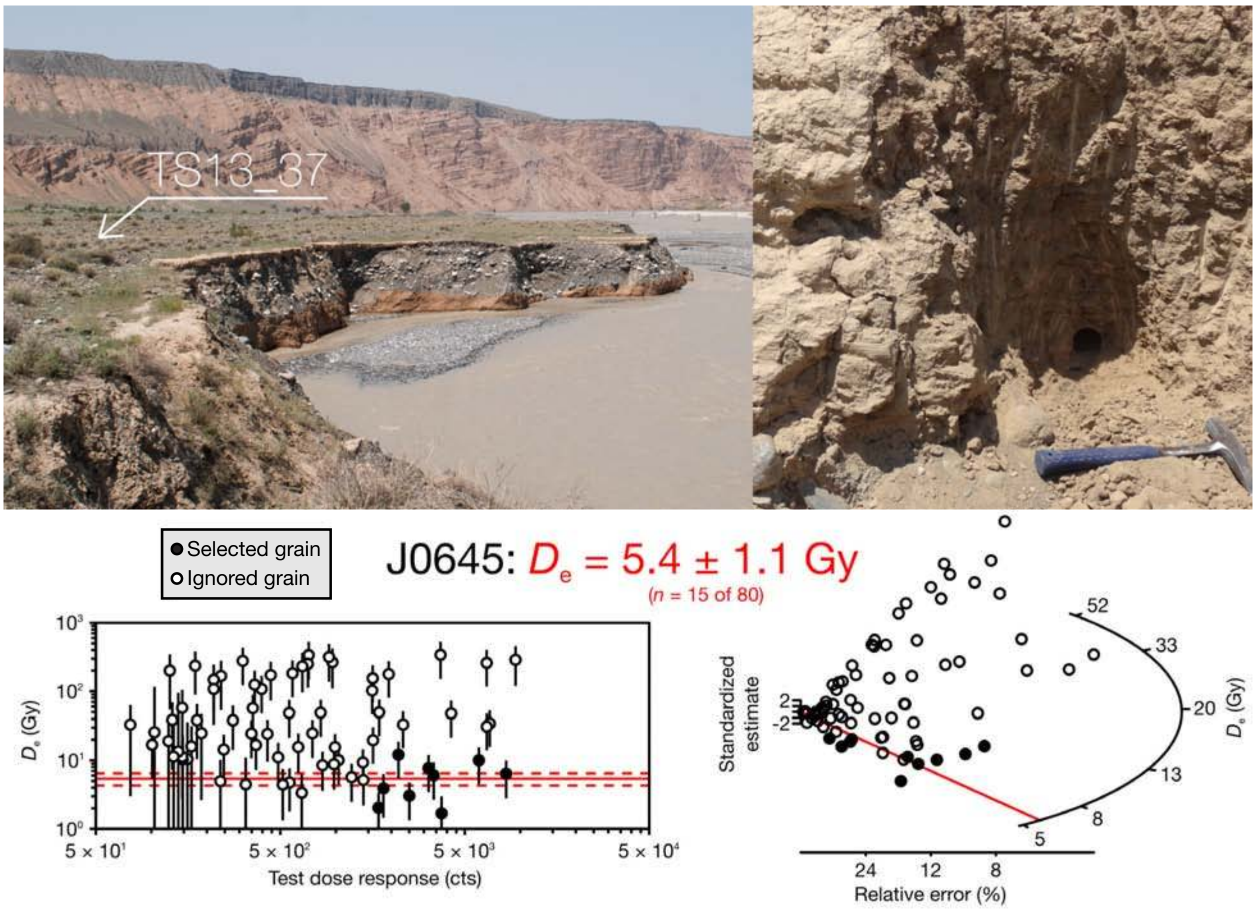

Figure 3: Location and details of sample **TS13_37 (J0645) = 1.7 ± 0.4 ka**; Kuitun; abandonment. Sample taken in 0.8 m of fluvially reworked clayey fine sand to silt with few granules. The sample was collected 5 cm above the fluvial fill. The fluvial fill is 3.2 m thick and lies on a bedrock strath of T2. On 3.7.2013, the strath was 1.6 m above the water level. The general approach for analysis is to reject grains based on sensitivity and high outliers. The overdispersion is 0.54.

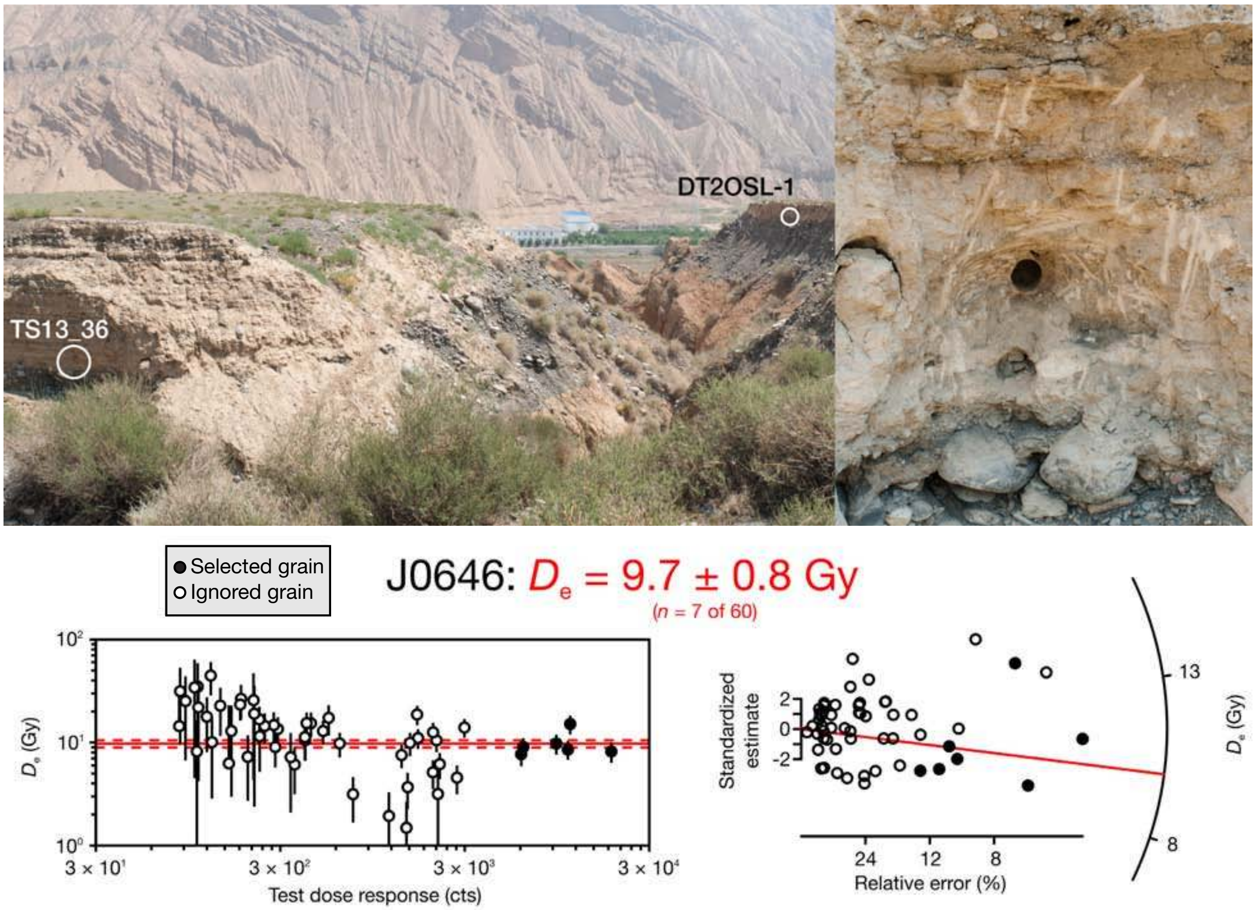

Figure 4: Location and details of sample **TS13_36 (J0646) = 3.3 ± 0.3 ka**; Kuitun; abandonment. Sample taken in the silt of a fluvially reworked 3.2 m thick series of loess and cross-bedded medium grained sand 20 cm above the top of the alluvial cobble conglomerate. The alluvial cobble conglomerate lies on the terrace strath and the sample constrains abandonment age. The general approach for analysis is to reject grains based on sensitivity. The overdispersion is 0.2.

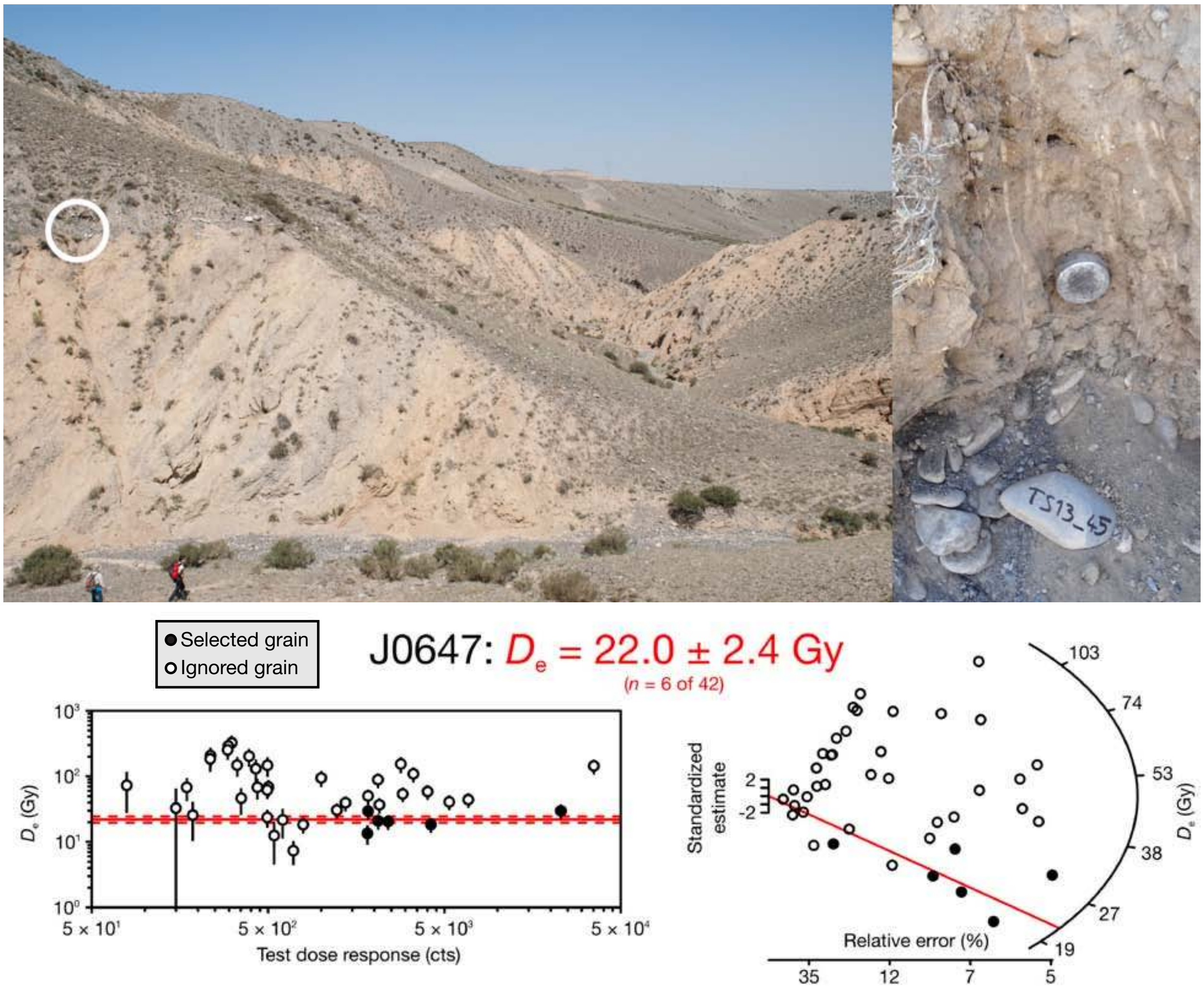

Figure 5: Location and details of sample **TS13_45 (J0647) = 7.7 ± 1.0 ka**; Kuitun; abandonment. Sample taken in the middle of the 0.3 m thick silt horizon capping the 1.5 m thick cobble conglomerate that lies on the strath of T7. The silt horizon is covered by a layer of creeping colluvium. It was not possible to dissociate the colluvium from the capping silt unequivocally. But it is very likely that the silt constrains the abandonment age of terrace T7.

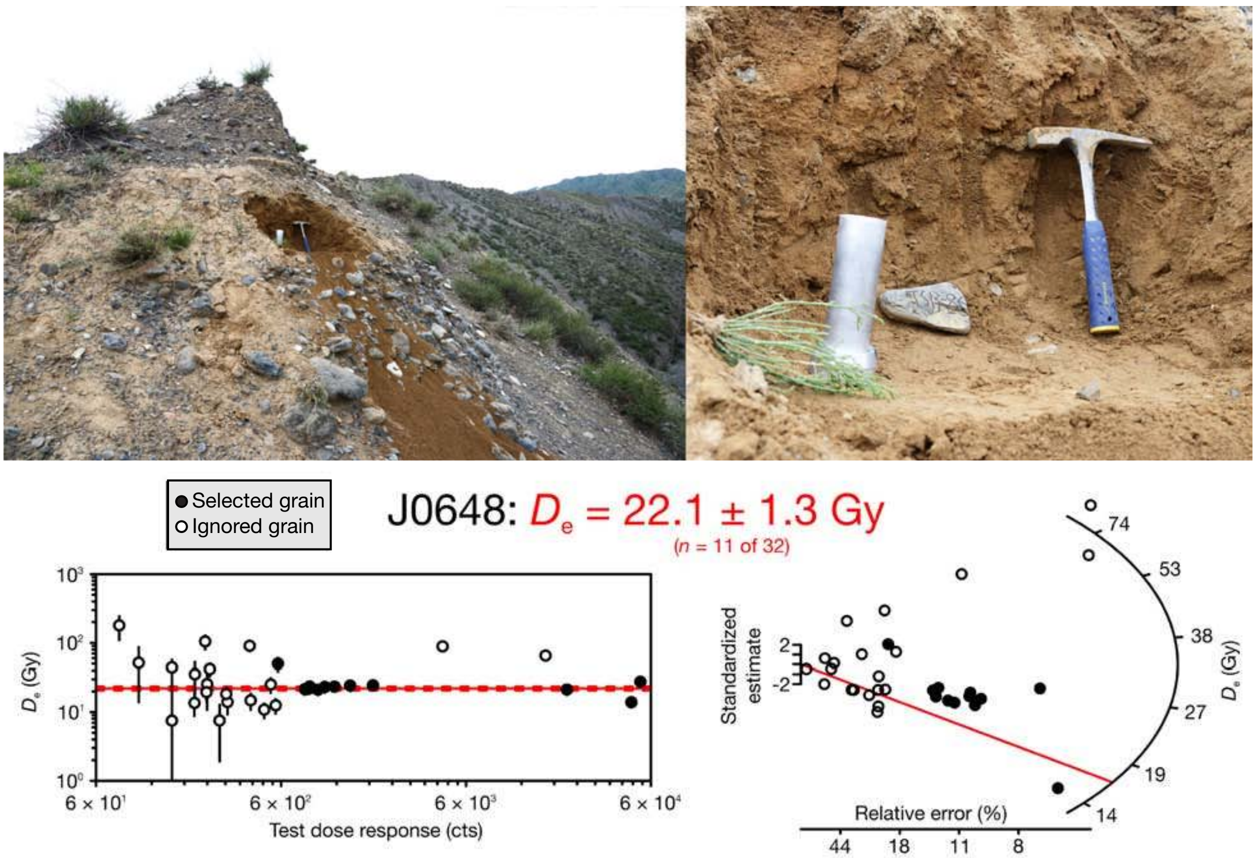

Figure 6: Location and details of sample **TS13_86 (J0648) = 8.4 ± 0.7 ka**; Kuitun; abandonment. The sample was taken in a silt horizon 20 cm above the fluvial deposit of the terrace and below a colluvium wedge. Although it appears from the pictures that the overlying coarse deposit might be fluvial and not colluvial. The sample would then reflect an aggradation age, not an abandonment.

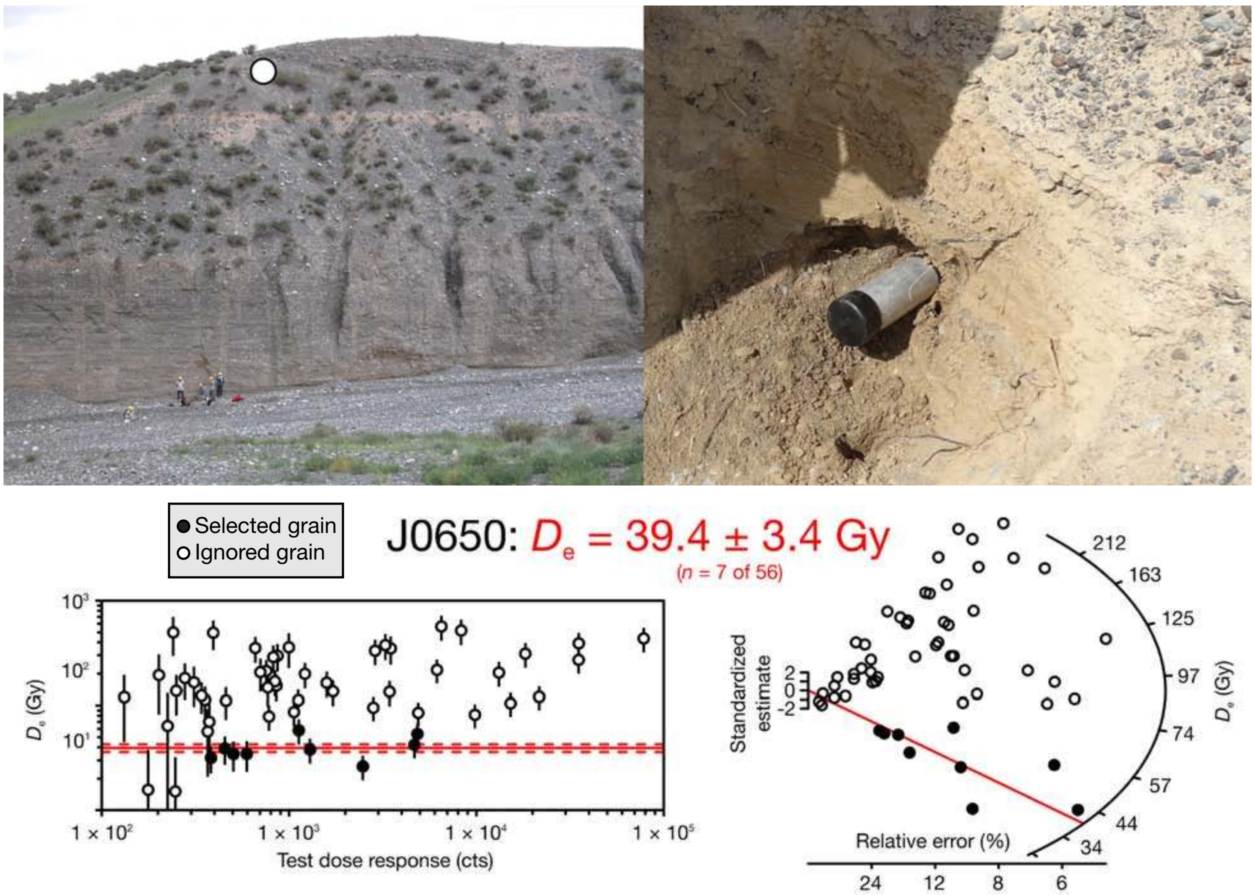

Figure 7: Location and details of sample **TS13_11 (J0650) = 13.4 ± 1.6 ka**; Kuitun; abandonment. Sample taken in a silt lens at the base of the colluvium wedge covering the alluvial cover of the terrace T9. It constrains the abandonment of T9 and it is a repeat of sample KTN-09 (10±2 ka) of Poisson and Avouac (2004).

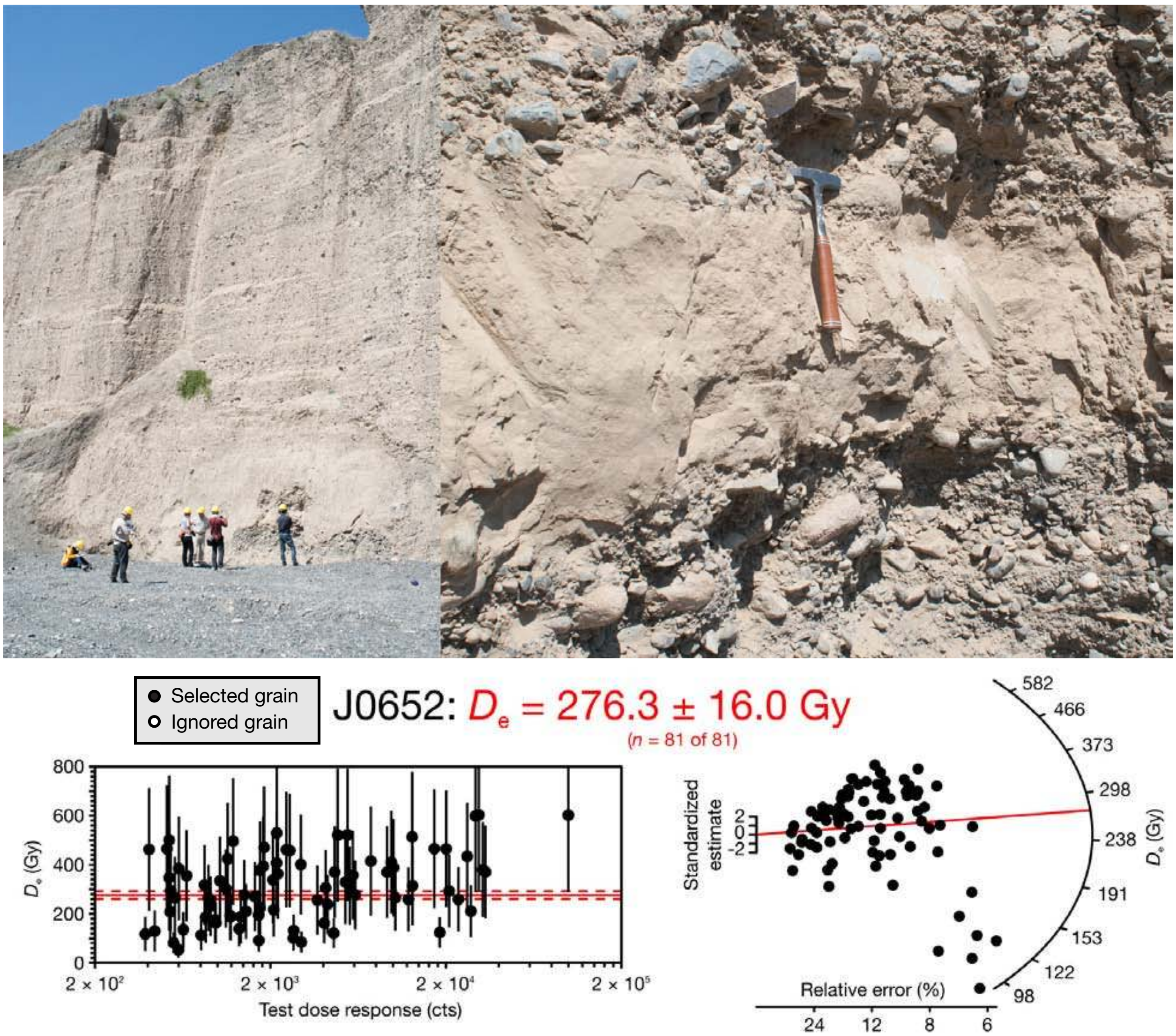

Figure 8: Location and details of sample **TS13_01 (J0652) = 116.8 ± 8.1 ka**; Kuitun; aggradation. Sample is collected at the base of the conglomerate cliff cut after abandonment of terrace T2. Material is a thick silt lens of reworked loess and very fine sand. The sample constrains a phase of aggradation of the alluvial fan. The overdispersion is 0.50.

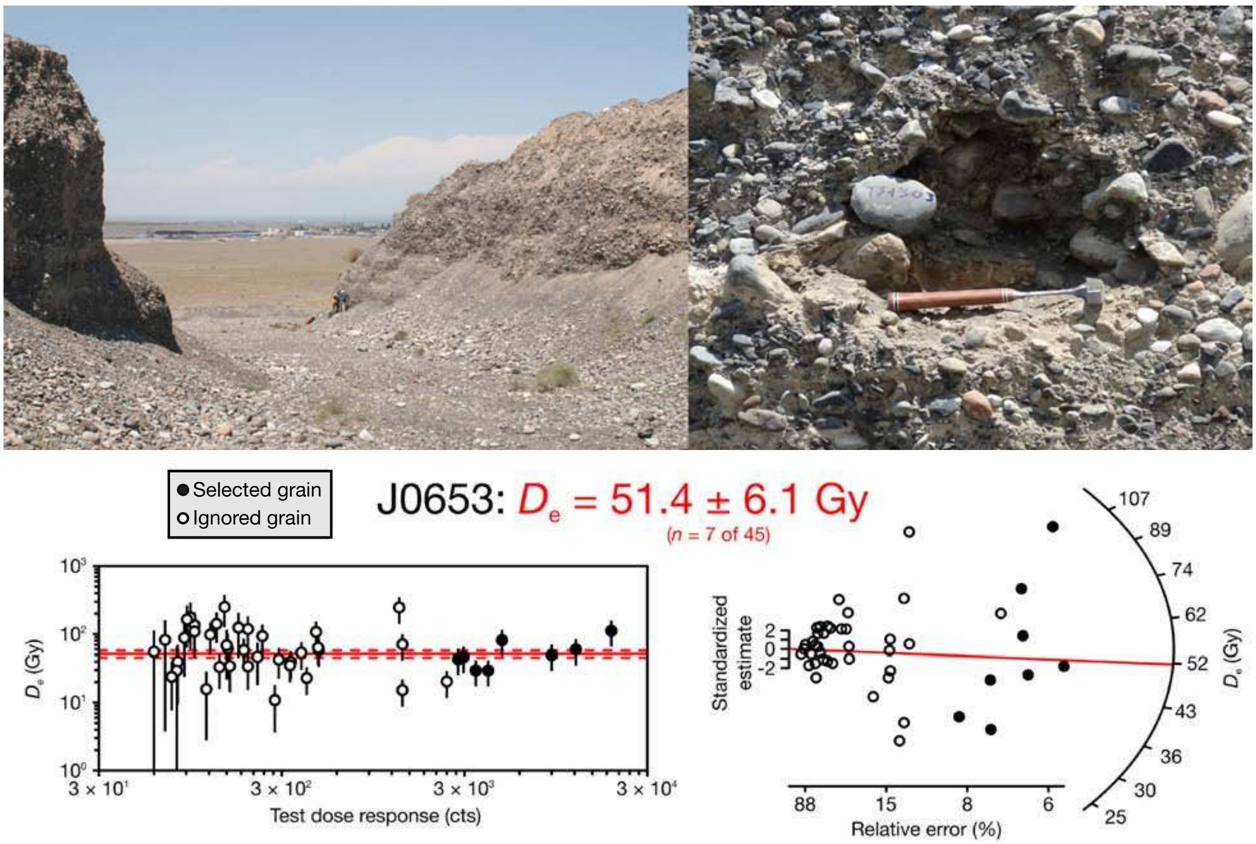

Figure 9: Location and details of sample **TS13_03 (J0653) = 18.3 ± 2.6 ka**; Kuitun; aggradation. Sample is collected in the riser of T3 at the downstream end of the Kuitun. Material is taken from a thin lens of silt. The sample constrains a phase of aggradation of the alluvial fan. The overdispersion is 0.33.

Figure 10: Picture looking East and down in the Swallow Canyon. The Kuitun Canyon, flowing from right to left, is visible in the background.

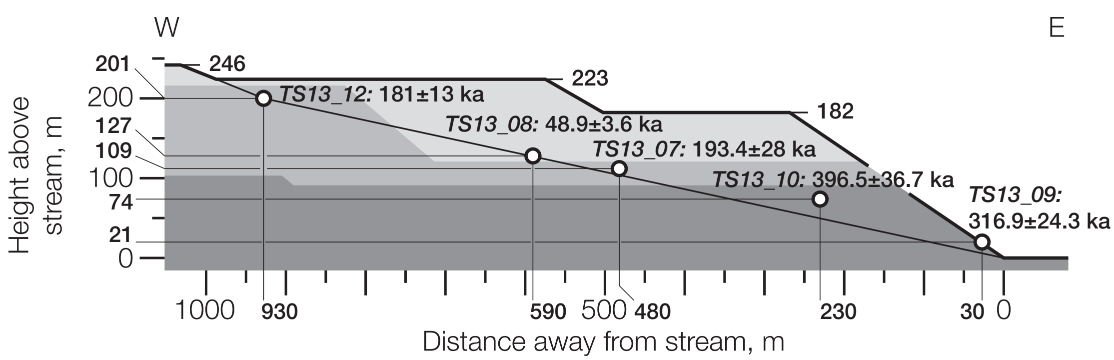

Figure 11: Schematic profile of the tributary Swallow Canyon and location of the samples TS13_12 (J0654), TS13_08 (J0655), TS13_07 (J0656), TS13_10 (J0657), TS13_09 (J0658). The shading represents a possible stratigraphy.

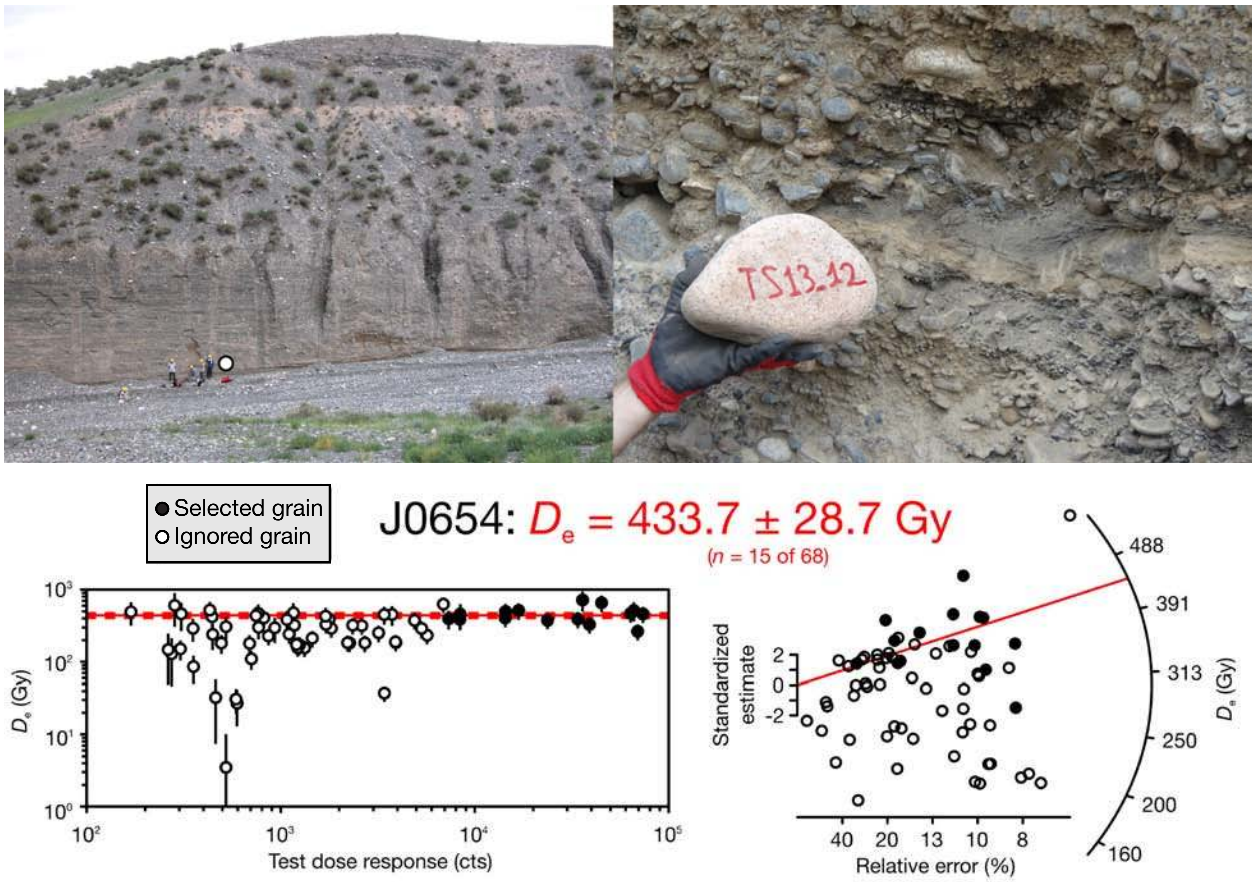

Figure 12: Location and details of sample **TS13_12 (J0654) = 181.0 ± 13.0 ka**; Kuitun; aggradation. Sample taken in a 10-15 cm thick lens of reworked silt to medium sand 201 m above the river. The sample constrains a phase of aggradation of the alluvial fan. The overdispersion is 0.25.

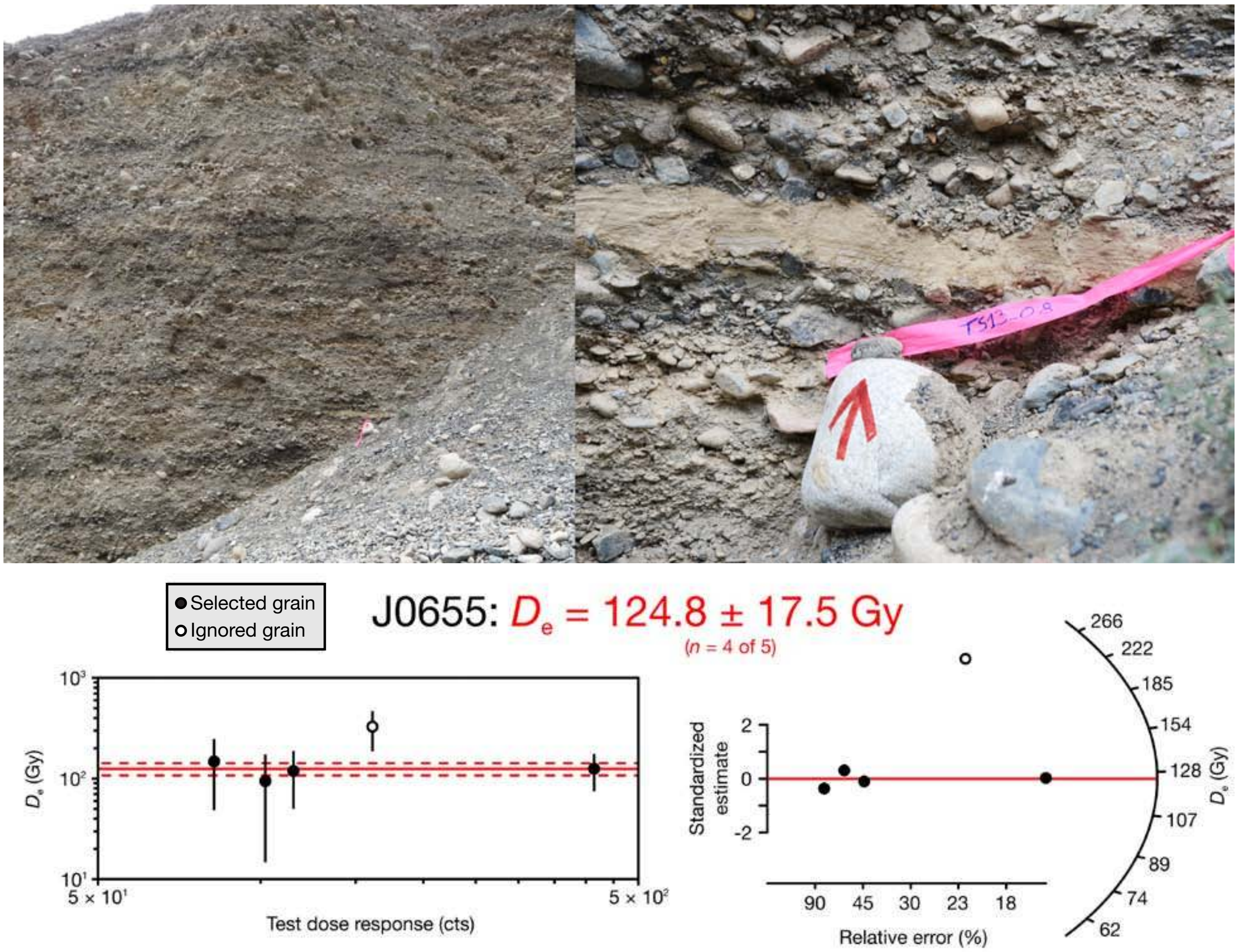

Figure 13: Location and details of sample **TS13_08 (J0655) = 48.9 ± 3.6 ka**; Kuitun; aggradation. Sample taken in a thin lens of reworked silt 127 m above the river. The sample constrains a phase of aggradation of the alluvial fan. The overdispersion is 0.42.

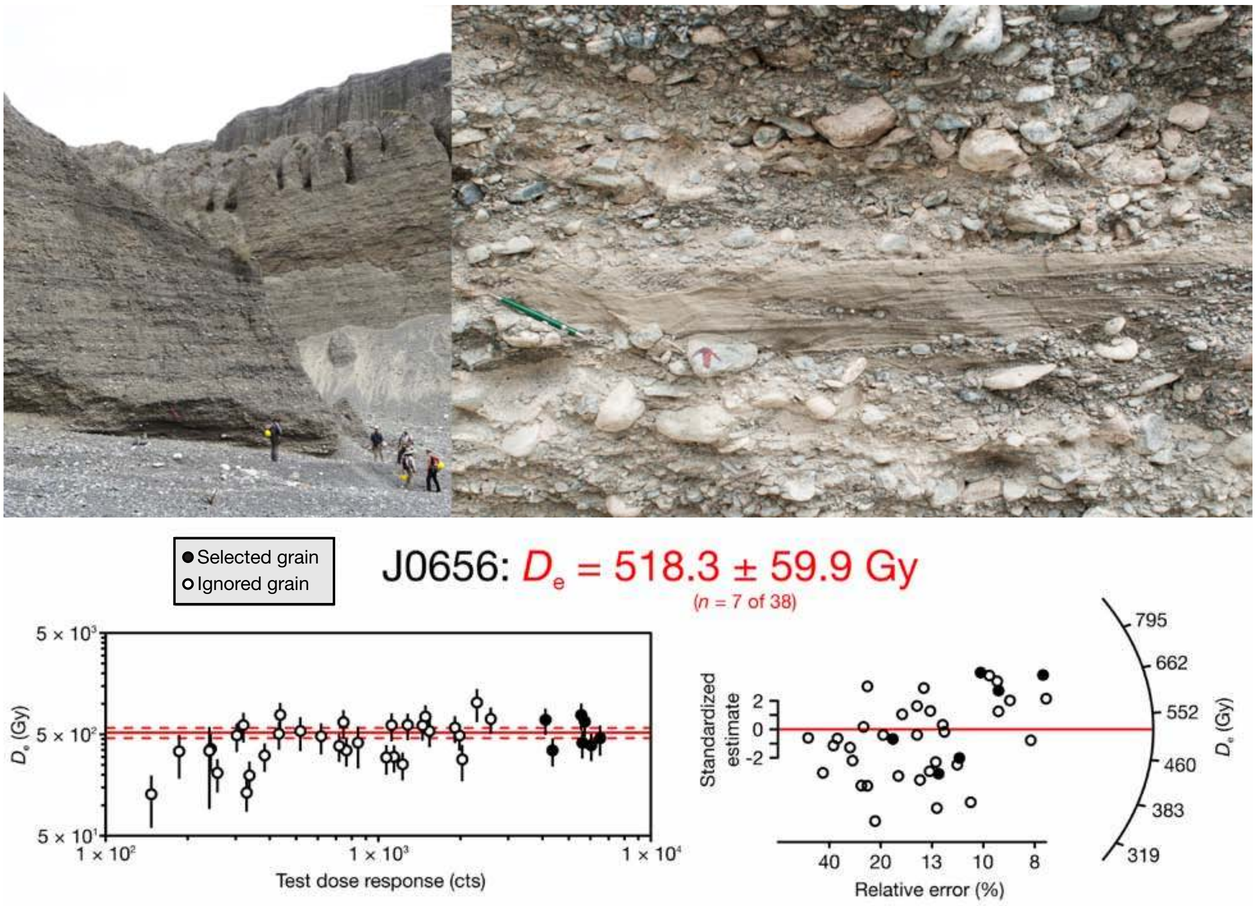

Figure 14: Location and details of sample **TS13_07 (J0656) = 193.4 ± 28.0 ka**; Kuitun; aggradation. Sample taken in a lens of reworked silt to fine sand 109 m above the river. The sample constrains a phase of aggradation of the alluvial fan. The overdispersion is 0.28.

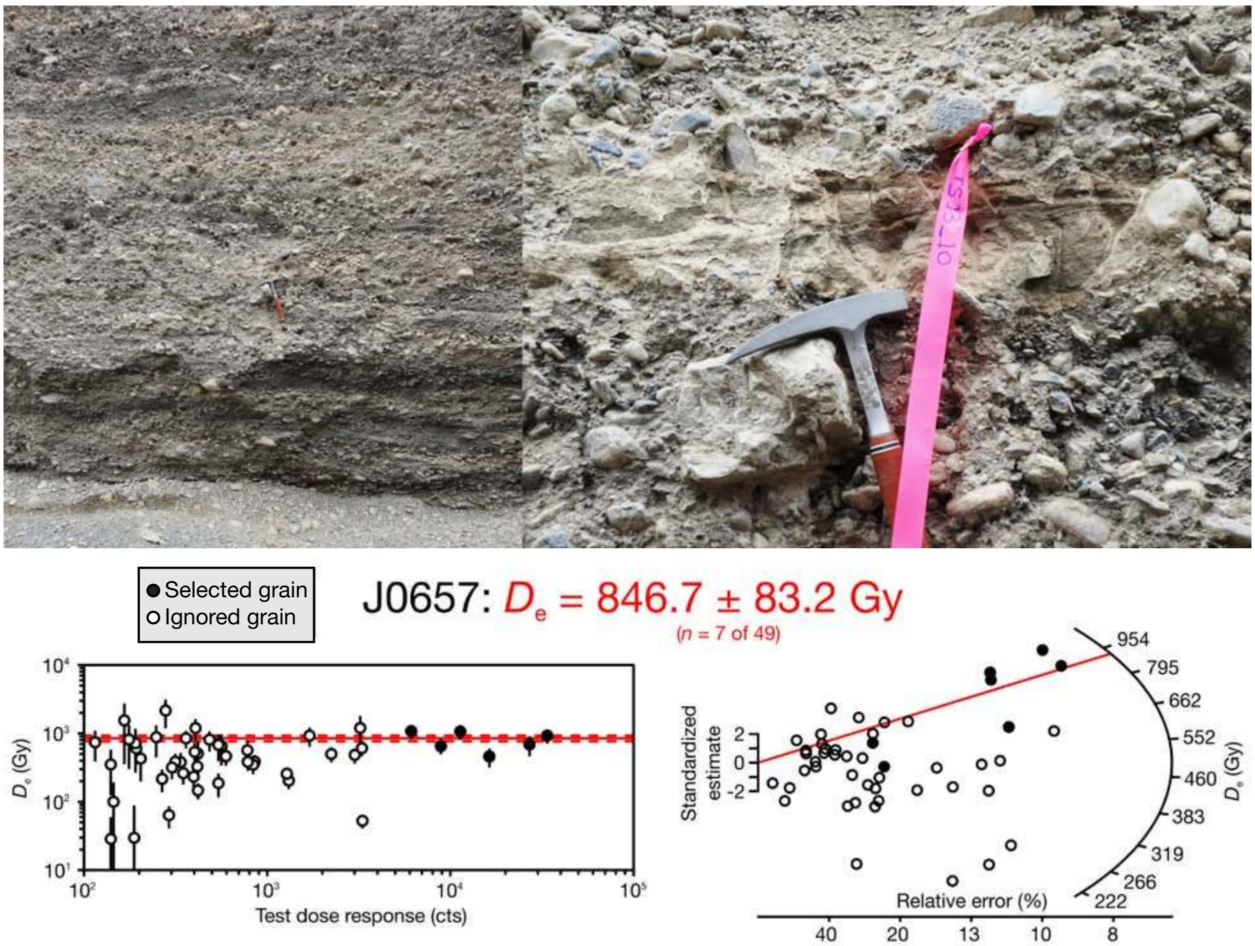

Figure 15: Location and details of sample **TS13_10 (J0657) = 396.5 ± 36.7 ka**; Kuitun; aggradation. Sample taken in a 10-15 cm thick lens of reworked silt to fine sand 74 m above the river. The sample constrains a phase of aggradation of the alluvial fan. The overdispersion is 0.22.

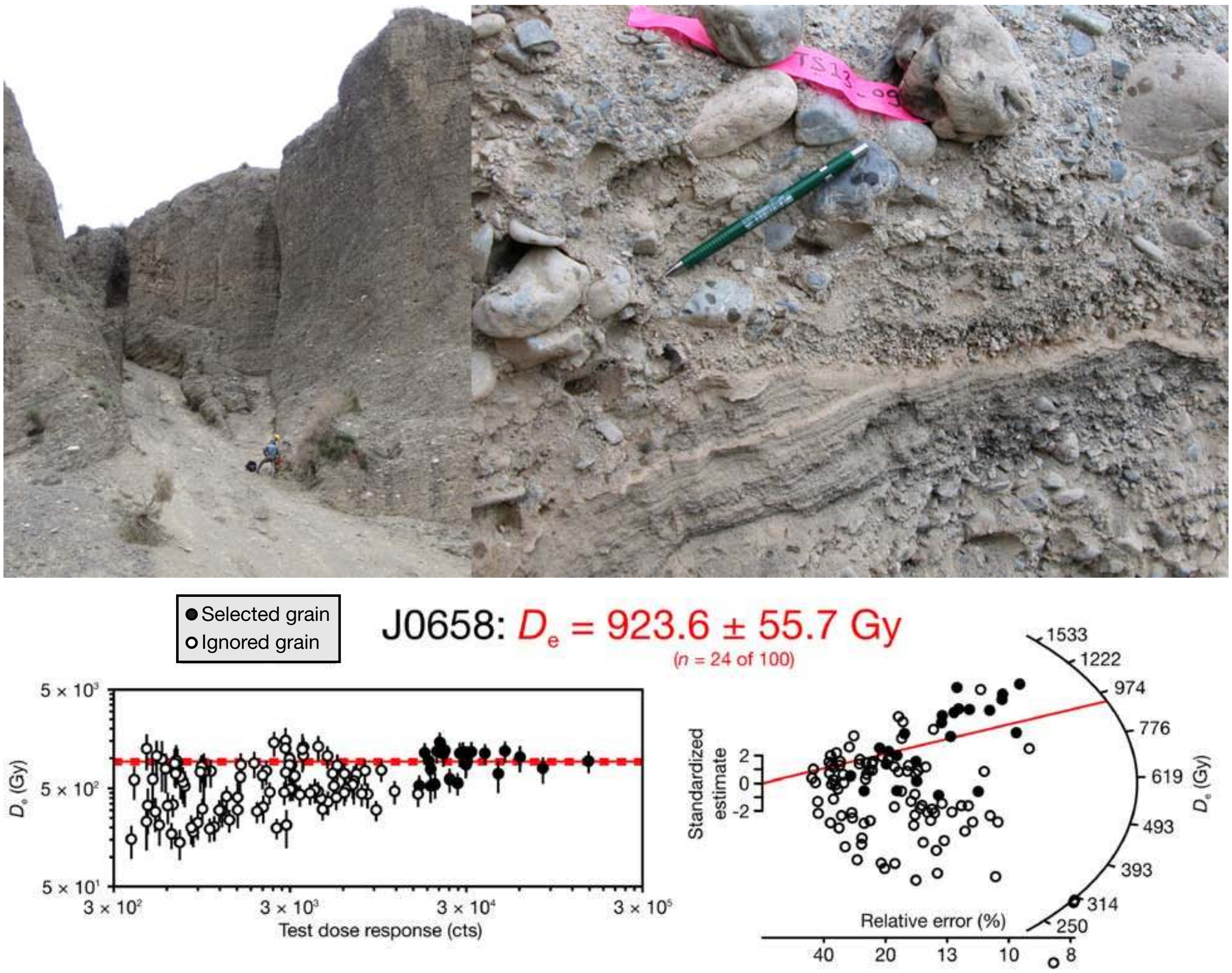

Figure 16: Location and details of sample **TS13_09 (J0658) = 316.9 ± 24.3 ka**; Kuitun; aggradation. Sample taken in a thin lens of reworked silt to medium sand 21 m above the river. The sample constrains a phase of aggradation of the alluvial fan. The overdispersion is 0.25.

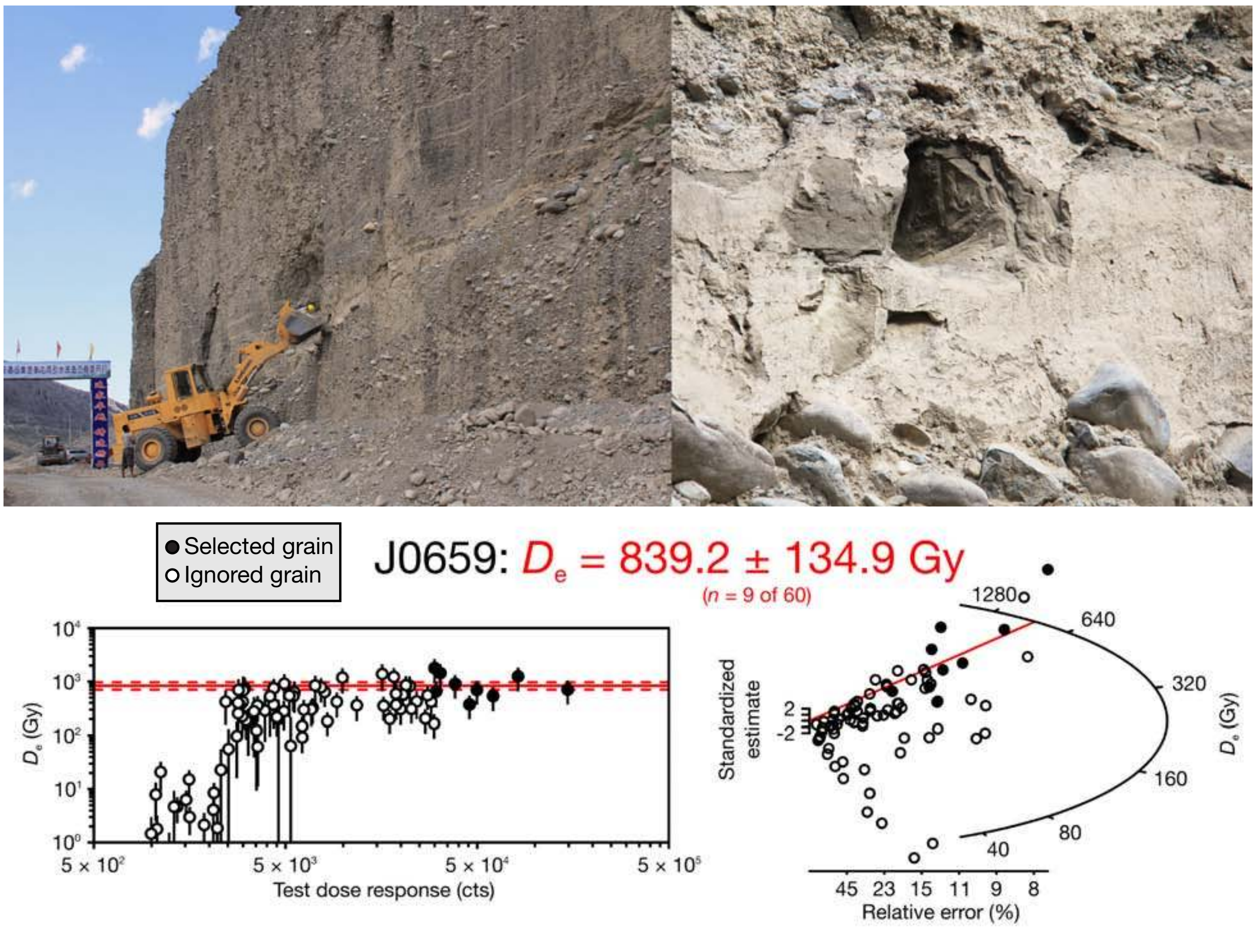

Figure 17: Location and details of sample **TS13_02 (J0659) = 286.1 ± 40.9 ka**; Kuitun; aggradation. Sample is collected at the base of the Kuitun main conglomerate cliff that is cut by Holocene incision, >250 m below the alluvial fan surface. Material is taken from a 1-1.5m thick loess horizon. The overdispersion is 0.46.

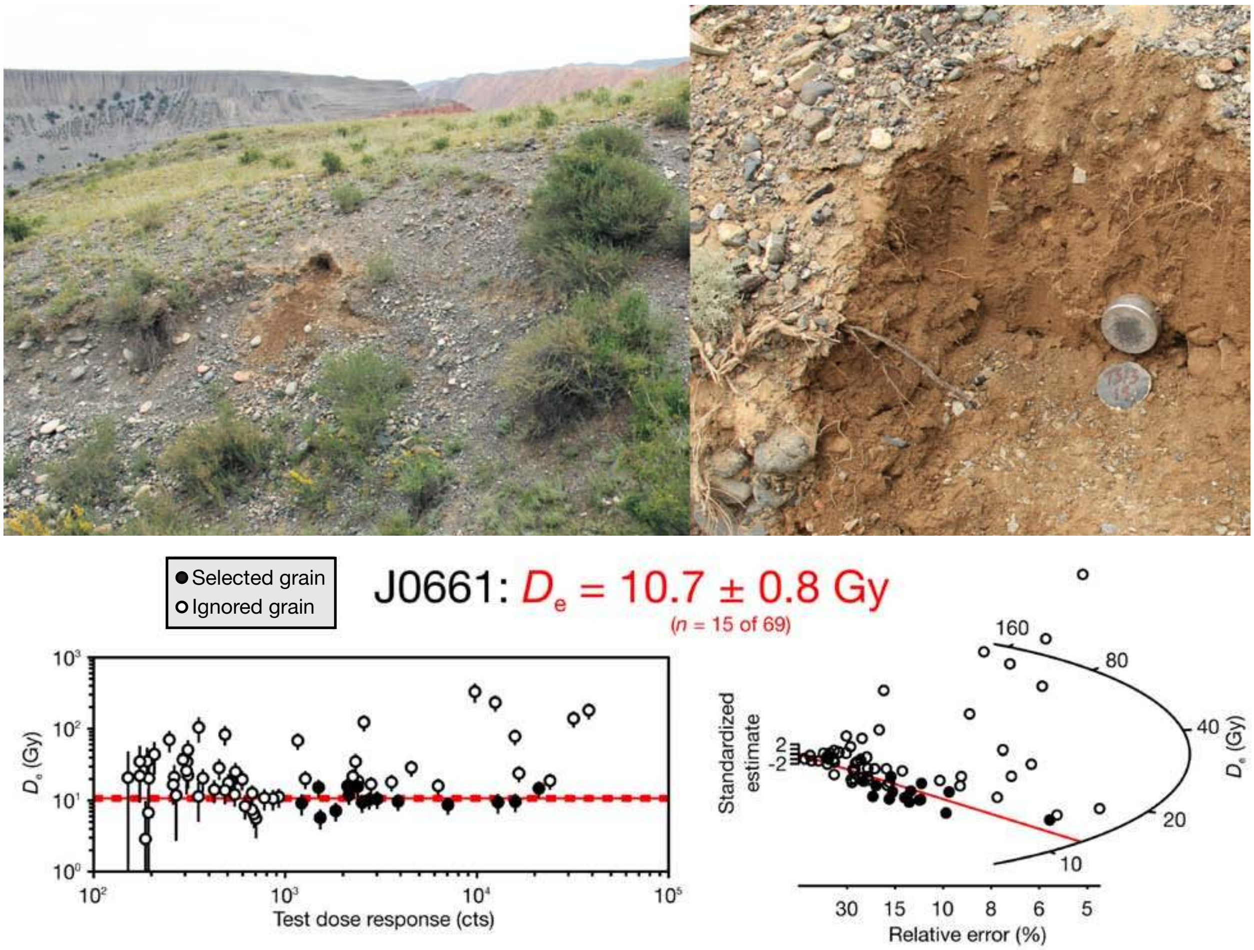

Figure 18: Location and details of sample **TS13_19 (J0661) = 3.6 ± 0.3 ka**; Anjihai; abandonment. Sample taken in a fine sand bed capping the fluvial deposits of terrace T13. The sample should constrain the abandonment of T13.

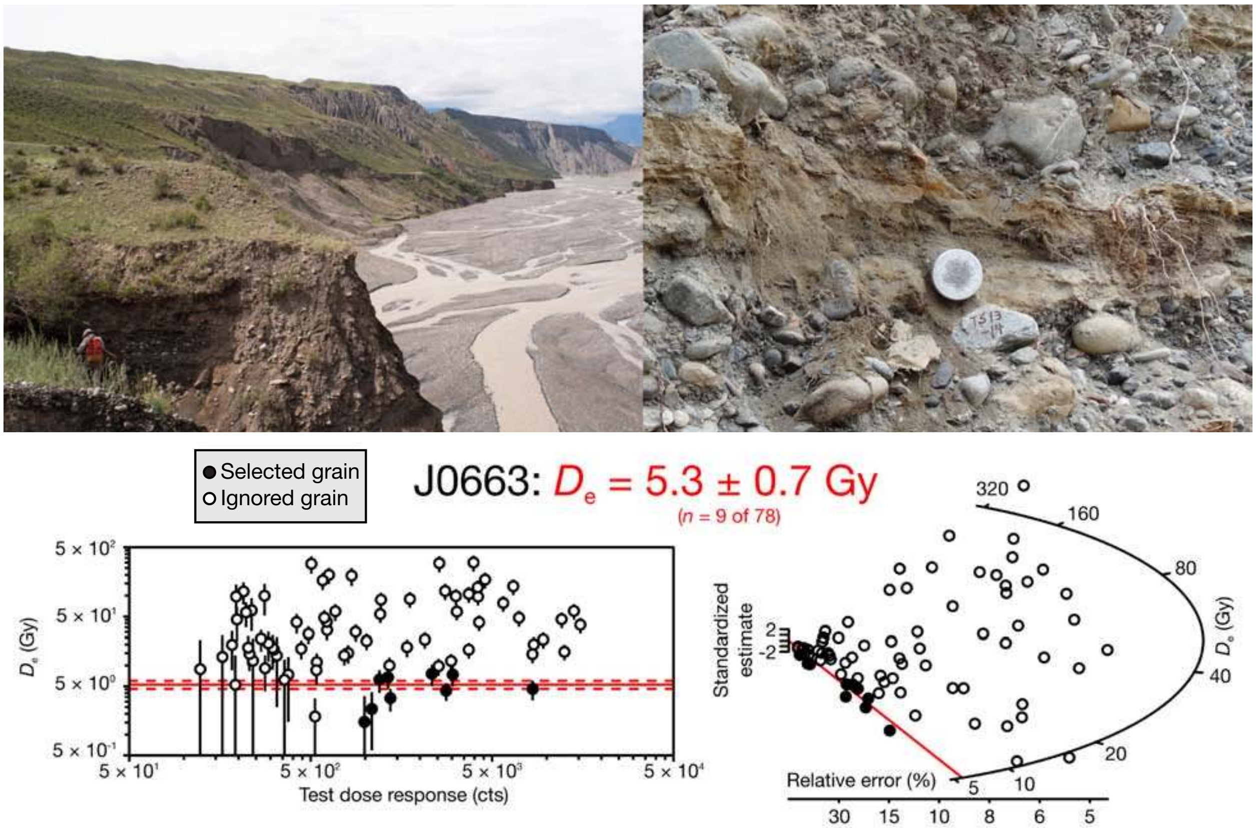

Figure 19: Location and details of sample **TS13_14 (J0663) = 1.7 ± 0.3 ka**; Anjihai; sample taken in a lens of reworked silt to fine sand at 0.8 m depth in the alluvial fill under terrace T2. The sample will provide an age constrain on the Anjihai alluvial fan aggradation.

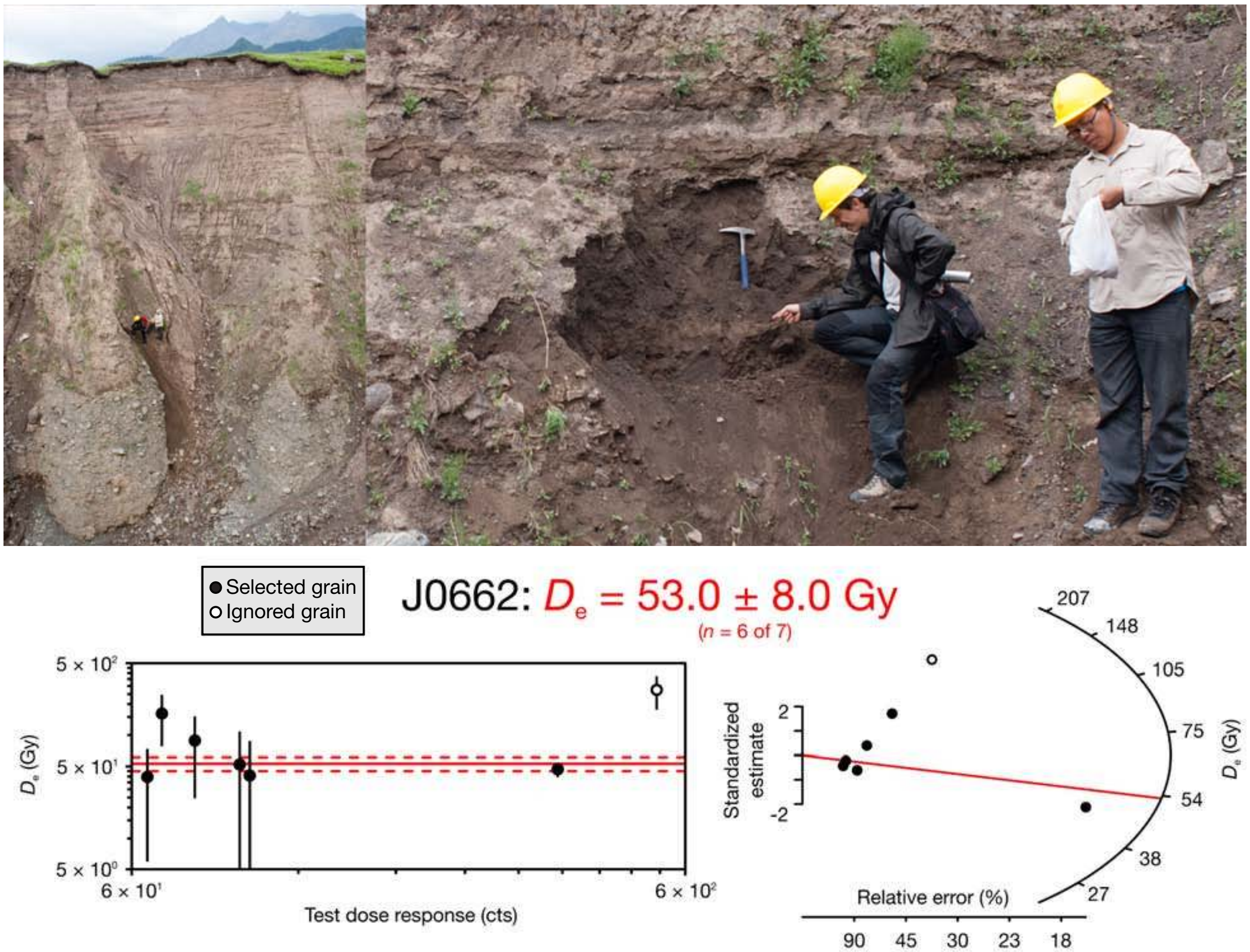

Figure 20: Location and details of sample **TS13_35 (J0662) = 37.4 ± 6.4 ka**; Toudao; abandonment. Sample taken in a silt horizon at the base of a ca. 10 m thick colluvial wedge, 5-10 cm above the top of the cobble conglomerate fill that defines the main terrace of the Toudao River. Sampling was done in a side wash cutting through the terrace. From this sample, we expect an abandonment constraint for the main terrace. The overdispersion is 0.

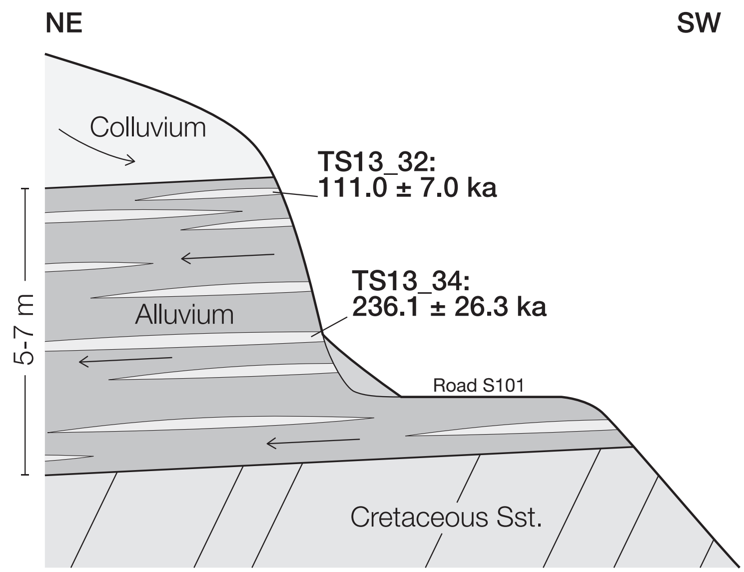

Figure 21: Stratigraphic relationship between **TS13_32 (J0665)** and **TS13_34 (J0664)**; Toudao; the samples are collected from silt lenses in an alluvial conglomerate that lies unconformable on Jurassic sandstone and is capped by colluvium.

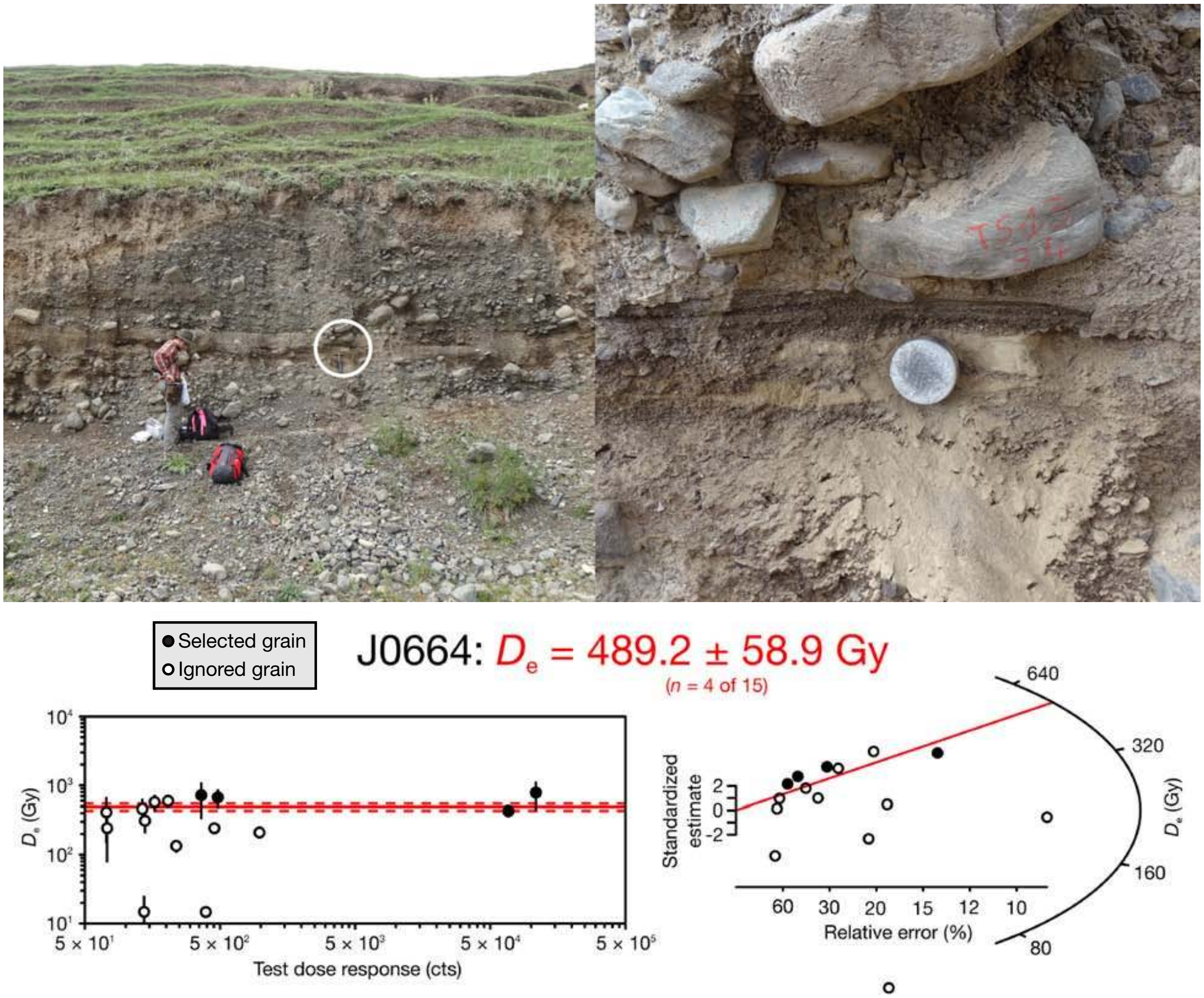

Figure 22: Location and details of sample **TS13_34 (J0664) = 236.1 ± 26.3 ka**; Toudao; Sample collected above the Toudao River in a narrow silty sand lens less than 10 cm thick, with granules and then pebbles and cobbles conglomerates above and below. The sample lies 2-3 m above the bedrock and 3-4 m below sample TS13_32, the two constrain the age of the fluvial deposit on the strath. See Figure 21 for a sketch of the stratigraphic relationship with TS13_32 (J0665). The overdispersion is 0.

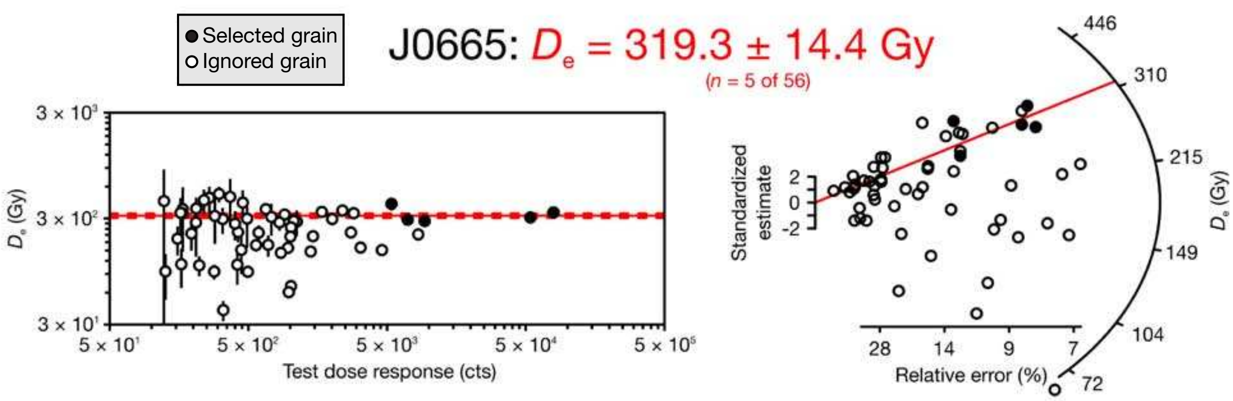

Figure 23: Location and details of sample **TS13_32 (J0665) = 111.0 ± 7.0 ka**; Toudao; abandonment. Sample taken in the first reworked silt lens above the massive fluvial cobble conglomerate and below a few thinner pebble conglomerate horizons. It represents the very last phase of aggradation that postdates the deposition of the main fill (cobble conglomerate) of this high terrace. The sample lies 3-4 m above TS13_34. See Figure 21 for a sketch of the stratigraphic relationship with TS13_34 (J0664). The overdispersion is 0.03.

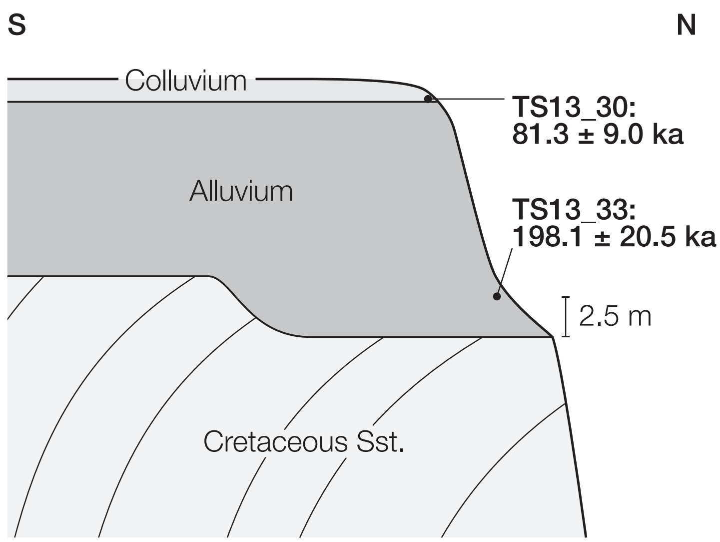

Figure 24: Stratigraphic relationship between **TS13_30 (J0668)** and **TS13_33 (J0669)**. The samples are collected from silt lenses in a thick alluvial conglomerate that lies unconformable on Jurassic sandstone and is capped by colluvium.

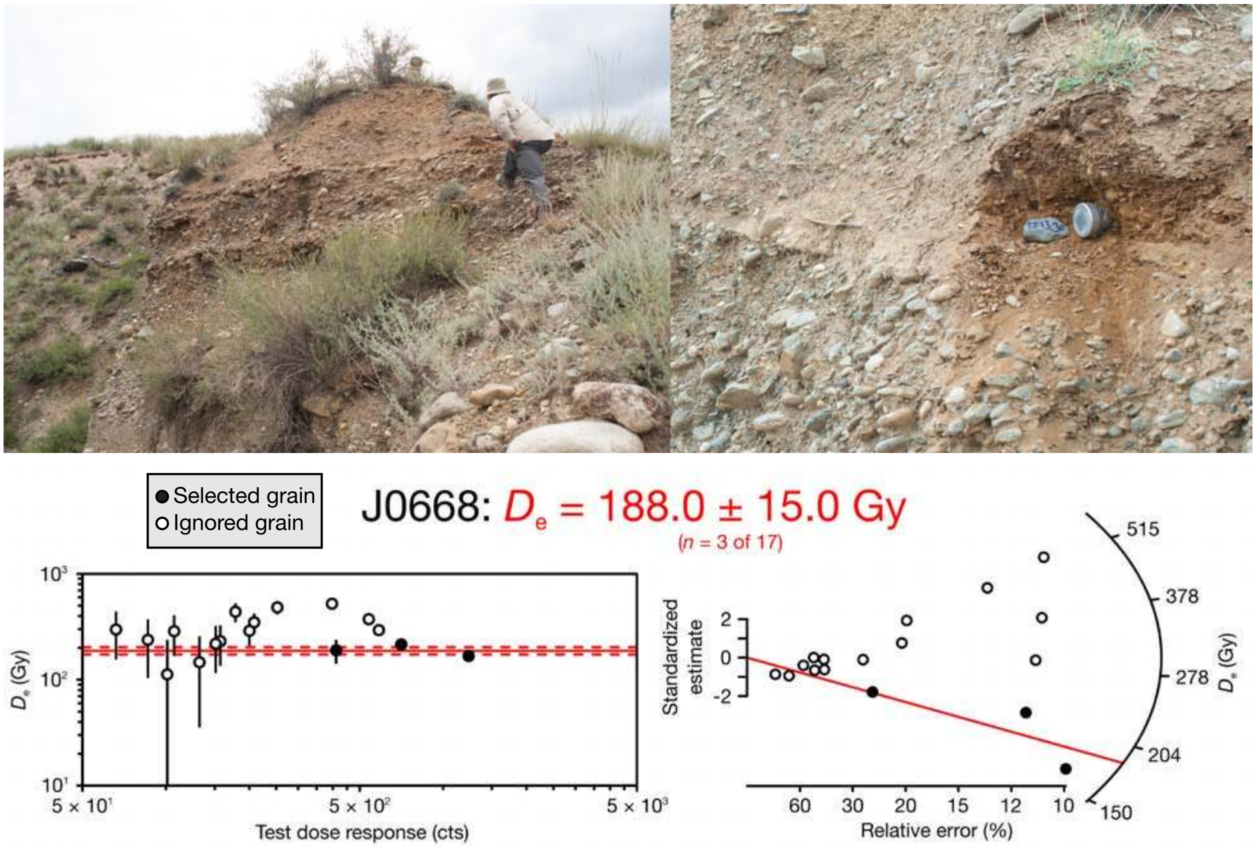

Figure 25: Location and details of sample **TS13_30 (J0668) = 81.3 ± 9.0 ka**; Manas; abandonment. The sample is in front of Jiawei Pan in the left picture. The sample was collected in the clay to fine sand capping the fluvial cobble-pebble deposits of the main strath terrace in the Upper Manas). This bed is covered by angular to subangular cobble-pebble colluvium and soil. The sample should constrain the age of the Upper Manas strath terrace. See Figure 24 for a sketch of the stratigraphic relationship with TS13_33 (J0669). The overdispersion is 0.05.

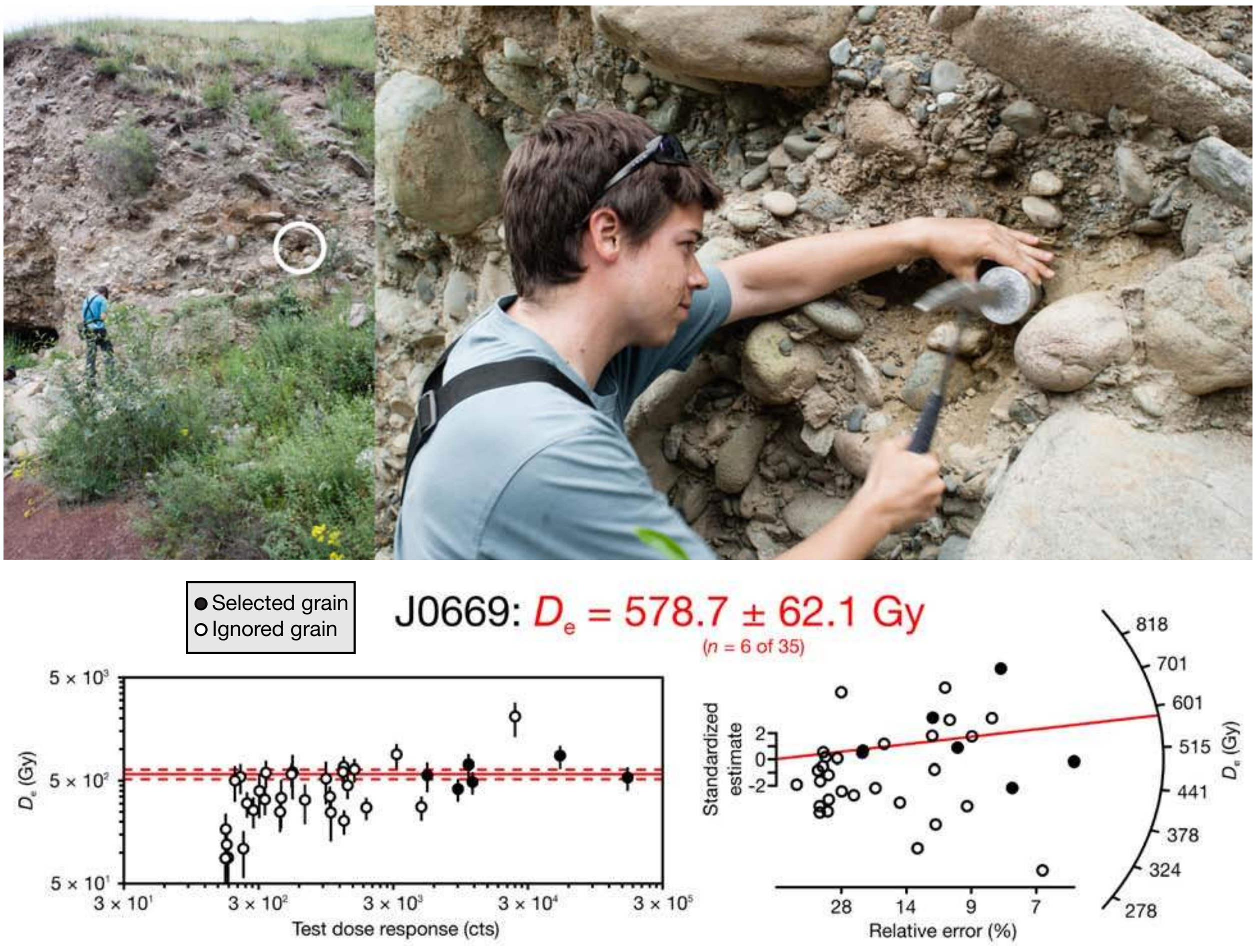

Figure 26: Location and details of sample **TS13_33 (J0669) = 198.1 ± 20.5 ka**. Sample taken in a very small clayey silt in the boulder conglomerate of the main strath terrace of the Upper Manas. The sample lies 2.5 m above the strath. It is a good constraint on the creation of the strath (assuming that the boulder conglomerate present today is the original cover of the strath). See Figure 24 for a sketch of the stratigraphic relationship with TS13_30 (J0668). The overdispersion is 0.24.

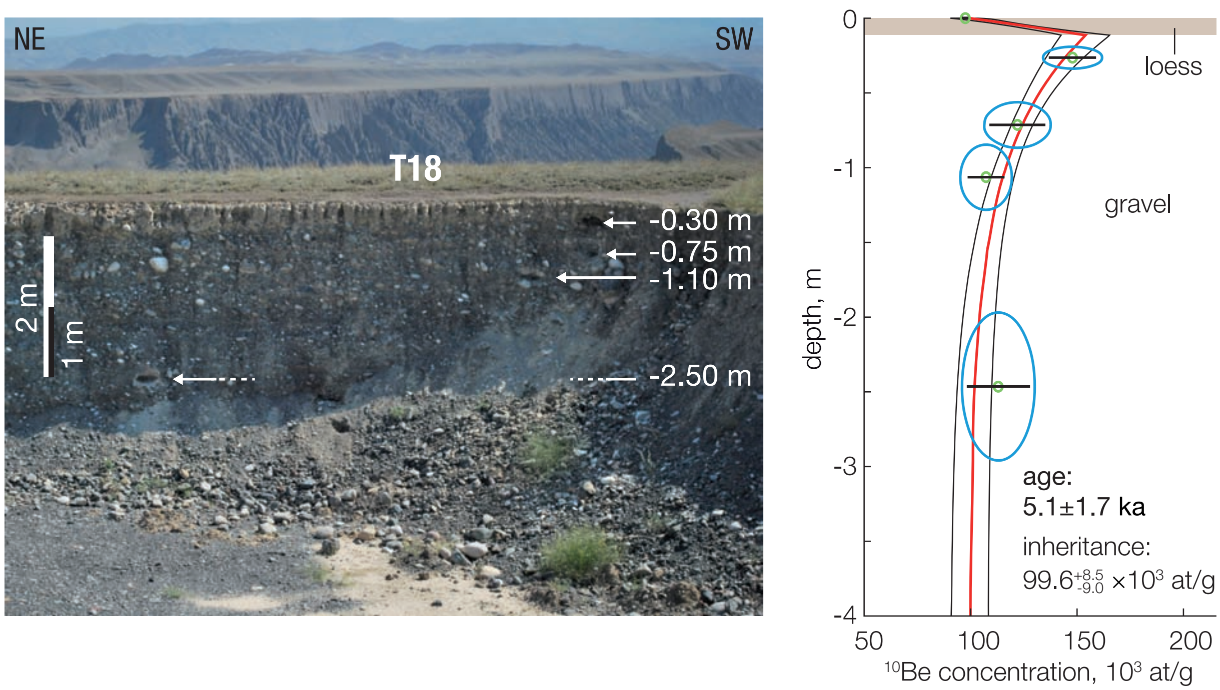

Figure 27: Left: sampling site for the depth profile analysis of sample **TS12_ANJ_T1B** = **5.1 ± 1.7 ka**. Right: ^{10}Be cosmogenic concentrations as a function of depth. The red line show the best fit model. Fine sediments (silt, loess, soil) are assumed to have a bulk density of 1.6±0.2 g/cm^3. The measured depths are converted to theoretical depths with the respective densities (blue ellipses).

Table 4: Supplementary Table Compilation of all published ages dating surfaces of the north alluvial piedmont of the Eastern Tian Shan. The map no. column lists the numbering used in the maps ("e" for external source). The relative height* is the elevation of the sample above the river divided by the height of the fill terrace marking the incision onset. Easting and Northing are referenced in the UTM zone 45 T. The River acronyms are ANJ (Anjihai), ANJw (Anjihai windgap), HTB (Hutubi), JNG (Jingou), KTN (Kuitun), MNS (Manas), TDO (Toudao), TSH (Tashi), and URQ (Urumqi). The sources are 1: this study; 2: Poisson and Avouac (2004); 3: Poisson (2002); 4: Gong et al. (2014); 5: Lu et al. (2014);6: Lu et al. (2010); 7: Stockmeyer, *in review*; 8: Fu et al. (2017). * Combination of the surface F_2 samples following Lu et al. (2010, p. 348). † These samples are not included in Figures 13 and 14 because they only border a small ephemeral stream that crosses the windgap after it was abandonment by the Anjihai River. The coordinates for Fu et al. (2017) listed here are the mean positions of the samples that contribute to each age.

River	**Map code**	**Sample no.**	**Age (ka)**	**Height***	**Lat. (°N)**	**Lon. (°E)**	**Method**
KTN	01	TS13_01[1]	116.8±8.1	0.10	44.3260	84.7793	p-IR IRSL
KTN	02	TS13_02[1]	286.1±40.9	0.05	44.1408	84.7354	p-IR IRSL
KTN	03	TS13_03[1]	18.3±2.6	0.67	44.3685	84.7927	p-IR IRSL
KTN	07	TS13_07[1]	193.4±28.0	0.44	44.2146	84.7740	p-IR IRSL
KTN	08	TS13_08[1]	48.9±3.6	0.52	44.2150	84.7729	p-IR IRSL
KTN	09	TS13_09[1]	316.9±24.3	0.09	44.2154	84.7806	p-IR IRSL
KTN	10	TS13_10[1]	396.5±36.7	0.30	44.2143	84.7771	p-IR IRSL
KTN	11	TS13_11[1]	13.4±1.6	1.00	44.2123	84.7672	p-IR IRSL
KTN	12	TS13_12[1]	181±13.0	0.82	44.2121	84.7669	p-IR IRSL
ANJ	14	TS13_14[1]	1.7±0.3	0.16	44.1008	85.0983	p-IR IRSL
ANJ	19	TS13_19[1]	3.6 ±0.3	0.88	44.0929	85.0986	p-IR IRSL
MNS	30	TS13_30[1]	81.3 ±9.0	0.95	43.8489	85.8011	p-IR IRSL
TDO	32	TS13_32[1]	111±7.0	1.00	43.9734	85.1261	p-IR IRSL
MNS	33	TS13_33[1]	198.1±20.5	0.80	43.8489	85.8013	p-IR IRSL
TDO	34	TS13_34[1]	236.1±26.3	1.00	43.9738	85.1255	p-IR IRSL
TDO	35	TS13_35[1]	37.4±6.4	1.00	43.9794	85.1071	p-IR IRSL
KTN	36	TS13_36[1]	3.3±0.3	0.32	44.2919	84.7873	p-IR IRSL
KTN	37	TS13_37[1]	1.7±0.4	0.02	44.2962	84.7885	p-IR IRSL
KTN	45	TS13_45[1]	7.7±1.0	0.76	44.2885	84.7819	p-IR IRSL
KTN	86	TS13_86[1]	8.4±0.7	0.65	44.2900	84.7900	p-IR IRSL
ANJ	1B	TS12-ANJ-T1B[1]	5.1 ±1.7	1.00	44.1052	85.0973	TCN
KTN	e1	OSL-T2-1[2]	10 ±1	0.92	44.2142	84.7725	OSL
KTN	e2	OSL-T2-2[2]	10.8 ±2	0.92	44.2142	84.7725	OSL
KTN	e3	OSL-T4-1[2]	7.3 ±1	0.65	44.3242	84.7728	OSL
KTN	e4	OSL-T4-2[2]	6.8 ±0.5	0.65	44.3223	84.7735	OSL
KTN	e5	OSL-T4-3[2]	7.5 ±1	0.65	44.3222	84.7738	OSL
KTN	e6	C-T5-1[2]	3.3 ±0.1	0.32	44.3213	84.7789	^{14}C
KTN	e7	C-T5-2[2]	3.4 ±0.2	0.32	44.2997	84.7811	^{14}C
KTN	e8	KTN_01[3]	35 ±10	1.00	44.2713	84.7625	OSL

KTN	e9	KTN_02[3]	86 ±10	1.00	44.2894	84.7600	OSL
MNS	e10	T-6-loess-bottom[4]	19.9 ±1.5	1.00	44.1786	86.1401	p-IR IRSL
MNS	e11	T-5-loess-bottom[4]	12.4 ±0.8	0.83	44.1284	86.1064	p-IR IRSL
MNS	e12	T-4-loess-bottom[4]	4 ±0.4	0.58	44.1659	86.1172	p-IR IRSL
MNS	e13	T-3-loess-bottom[4]	3.1 ±0.3	0.44	44.1673	86.1155	p-IR IRSL
MNS	e14	T-2-loess-bottom[4]	1.4 ±0.3	0.22	44.1677	86.1139	p-IR IRSL
MNS	e15	T-1-loess-bottom[4]	0.5 ±0.1	0.11	44.1685	86.1114	p-IR IRSL
URQ	e16	4 (T7)[5]	255 -25/+15	1.00	43.4043	87.2149	OSL
URQ	e17	2 (T5)[5]	142 ±14	1.00	43.4867	87.3060	OSL
URQ	e18	1 (T2)[5]	3.52 ±0.04	0.73	43.5314	87.3304	^{14}C
mix	e19	2-3-4-5 ($F_2(T_2)$)[6*]	295 ±25	1.00	—	—	ESR
TSH	e20	1 ($T_3(F_3)$)[6]	1.8 ±0.2	0.16	44.1576	86.3416	OSL
TSH	e21	1 ($T_3(F_3)$)[6]	26 ±2.7	0.16	44.0122	86.3360	OSL
JNG	e22	3a ($T_3(F_3)$)[6]	28.7 ±3	0.80	44.1814	85.4513	OSL
JNG	e23	3b ($T_3(F_3)$)[6]	12.6 ±1.3	0.97	44.1814	85.4513	OSL
JNG	e24	TGL-T4[7]	19.6 +14.5/-8.3	1.00	44.0649	86.3351	p-IR IRSL
TSH	e25	TGL-T3[7]	42.8 +18.2-12.7	1.00	44.0709	86.3280	p-IR IRSL
TSH	e26	TGL-T2[7]	75.2 +31.7/-17.6	1.00	44.0647	86.3280	p-IR IRSL
TSH	e27	TGL-T1[7]	188.8 +62.8/-47.1	1.00	44.0673	86.3138	p-IR IRSL
TSH	e28	TGL-T0[7]	245.6 +72.3/-55.9	1.00	44.0686	86.3094	p-IR IRSL
ANJw	e29	AJH-02-04[8†]	3.6±0.1	1.00	∼44.27	∼85.17	OSL & p-IR IRSL
ANJw	e30	AJH-06,07,08[8†]	9.0±0.6	1.00	∼44.27	∼85.18	OSL & p-IR IRSL
ANJw	e31	AJH-08,09,11,12[8]	53.3±2.2	1.00	∼44.26	∼85.19	OSL & p-IR IRSL

References

G. Adamiec and M. J. Aitken. Dose-rate conversion factors: update. *Ancient TL*, pages 37–50, 1998.

M. J. Aitken. *Thermoluminescence Dating*. Academic Press, London, 1985.

G. Balco, J. Briner, R. C. Finkel, J. A. Rayburn, J. C. Ridge, and J. M. Schaefer. Regional beryllium-10 production rate calibration for late-glacial northeastern North America. *Quaternary Geochronology*, 4(2):93–107, Apr. 2009.

R. Braucher, D. L. Bourlès, E. T. Brown, F. Colin, J. P. Muller, J. J. Braun, M. Delaune, A. Edou Minko, C. Lescouet, G. M. Raisbeck, and F. Yiou. Application of in situ-produced cosmogenic 10Be and 26Al to the study of lateritic soil development in tropical forest: theory and examples from Cameroon and Gabon. *Chemical Geology*, 170(1-4):95–111, Oct. 2000.

R. Braucher, S. Merchel, J. Borgomano, and D. L. Bourlès. Production of cosmogenic radionuclides at great depth: A multi element approach. *Earth and Planetary Science Letters*, 309(1–2):1–9, 2011.

E. T. Brown, J. M. Edmond, G. M. Raisbeck, F. Yiou, M. D. Kurz, and E. J. Brook. Examination of surface exposure ages of Antarctic moraines using in situ produced 10Be and 26Al. *Geochimica Et Cosmochimica Acta*, 55(8):2269–2283, Aug. 1991.

N. D. Brown, E. J. Rhodes, J. L. Antinao, and E. V. McDonald. Single-grain post-IR IRSL signals of K-feldspars from alluvial fan deposits in Baja California Sur, Mexico. *Quaternary International*, 362:132–138, 2015.

J.-P. Buylaert, A. S. Murray, K. J. Thomsen, and M. Jain. Testing the potential of an elevated temperature IRSL signal from K-feldspar. *Radiation Measurements*, 44(5-6):560–565, May 2009.

J. Chmeleff, F. von Blanckenburg, K. Kossert, and D. Jakob. Determination of the 10Be half-life by multicollector ICP-MS and liquid scintillation counting. *Nuclear Instruments & Methods In Physics Research Section B-Beam Interactions With Materials And Atoms*, 268(2):192–199, Jan. 2010.

T. J. Dunai. *Cosmogenic Nuclides*. principles, concepts and applications in the earth surface sciences. Cambridge University Press, 2010.

X. Fu, S.-H. Li, B. Li, and B. Fu. A fluvial terrace record of late Quaternary folding rate of the Anjihai anticline in the northern piedmont of Tian Shan, China. *Geomorphology*, 278:91–104, Feb. 2017.

M. Fuchs and A. Lang. OSL dating of coarse-grain fluvial quartz using single-aliquot protocols on sediments from NE Peloponnese, Greece. *Quaternary Science Reviews*, 20(5-9):783–787, 2001.

R. F. Galbraith, R. G. Roberts, G. M. Laslett, H. Yoshida, and J. M. Olley. Optical dating of single and multiple grains of quartz from Jinmium rock shelter, northern Australia: Part I, experimental design and statistical models. *Archaeometry*, 41(2):339–364, 1999.

Z. Gong, S.-H. Li, and B. Li. The evolution of a terrace sequence along the Manas River in the northern foreland basin of Tian Shan, China, as inferred from optical dating . *Geomorphology*, 213(C):201–212, May 2014.

J. C. Gosse and F. Phillips. Terrestrial in situ cosmogenic nuclides: theory and application. *Quaternary Science Reviews*, 20(14):1475–1560, 2001.

B. Guralnik, A. Matmon, Y. Avni, N. Porat, and D. Fink. Constraining the evolution of river terraces with integrated OSL and cosmogenic nuclide data. *Quaternary Geochronology*, 6(1): 22–32, 2011.

G. S. Hancock, R. S. Anderson, O. A. Chadwick, and R. C. Finkel. Dating fluvial terraces with Be-10 and Al-26 profiles: application to the Wind River, Wyoming. *Geomorphology*, 27(1-2): 41–60, Feb. 1999.

D. J. Huntley. An explanation of the power-law decay of luminescence. *Journal of Physics: Condensed Matter*, 18(4):1359–1365, 2006.

D. J. Huntley and M. R. Baril. The K content of the K-feldspars being measured in optical dating or in thermoluminescence dating. *Ancient TL*, 15(1):11–13, 1997.

D. J. Huntley and M. Lamothe. Ubiquity of anomalous fading in K-feldspars and the measurement and correction for it in optical dating. *Canadian Journal of Earth Sciences*, 38(7):1093–1106, 2001.

R. H. Kars, J. Wallinga, and K. M. Cohen. A new approach towards anomalous fading correction for feldspar IRSL dating–tests on samples in field saturation. *Radiation Measurements*, 43(2-6): 786–790, 2008.

R. H. Kars, T. Reimann, C. Ankjaergaard, and J. Wallinga. Bleaching of the post-IR IRSL signal: new insights for feldspar luminescence dating. *Boreas*, 43(4):780–791, 2014.

C. P. Kohl and K. Nishiizumi. Chemical isolation of quartz for measurement of in-situ-produced cosmogenic nuclides. *Geochimica Et Cosmochimica Acta*, 1992.

G. Korschinek, A. Bergmaier, T. Faestermann, U. C. Gerstmann, K. Knie, G. Rugel, A. Wallner, I. Dillmann, G. Dollinger, C. L. von Gostomski, K. Kossert, M. Maiti, M. Poutivtsev, and A. Remmert. A new value for the half-life of 10Be by Heavy-Ion Elastic Recoil Detection and liquid scintillation counting. *Nuclear Instruments & Methods In Physics Research Section B-Beam Interactions With Materials And Atoms*, 268(2):187–191, Jan. 2010.

S. Kreutzer, C. Schmidt, M. C. Fuchs, M. Dietze, M. Fischer, and M. Fuchs. Introducing an R package for luminescence dating analysis. *Ancient TL*, 30(1):1–8, 2012.

D. Lal. Cosmic-Ray Labeling of Erosion Surfaces - Insitu Nuclide Production-Rates and Erosion Models. *Earth and Planetary Science Letters*, 104:424–439, 1991.

M. Lamothe, M. Auclair, C. Hamzaoui, and S. Huot. Towards a prediction of long-term anomalous fading of feldspar IRSL. *Radiation Measurements*, 37(4-5):493–498, 2003.

B. Li and S.-H. Li. Luminescence dating of K-feldspar from sediments: A protocol without anomalous fading correction. *Quaternary Geochronology*, 6(5):468–479, 2011.

H. Lu, D. W. Burbank, and Y. Li. Alluvial sequence in the north piedmont of the Chinese Tian Shan over the past 550 kyr and its relationship to climate change. *Palaeogeography Palaeoclimatology Palaeoecology*, 285(3-4):343–353, Jan. 2010.

H. Lu, T. Zhang, J. Zhao, S. Si, H. Wang, S. Chen, and X. Zheng. Late Quaternary alluvial sequence and uplift-driven incision of the Urumqi River in the north front of the Tian Shan, northwestern China. *Geomorphology*, 219:141–151, 2014.

K. Nishiizumi, M. Imamura, M. W. Caffee, J. R. Southon, R. C. Finkel, and J. McAninch. Absolute calibration of 10Be AMS standards. *Nuclear Instruments & Methods In Physics Research Section B-Beam Interactions With Materials And Atoms*, 258(2):403–413, May 2007.

B. Poisson. *Impact du climat et de la tectonique sur l'évolution géomorphologique d'un piémont: exemple du piémont Nord du Tian Shan depuis la fin du Pléistocène* . PhD thesis, Université Paris XI, 2002.

B. Poisson and J.-P. Avouac. Holocene hydrological changes inferred from alluvial stream entrenchment in North Tian Shan (Northwestern China). *Journal of Geology*, 112(2):231–249, 2004.

J. R. Prescott and J. T. Hutton. Cosmic ray contributions to dose rates for luminescence and ESR dating: Large depths and long-term time variations. *Radiation Measurements*, 23(2-3):497–500, 1994.

E. J. Rhodes. Dating sediments using potassium feldspar single-grain IRSL: initial methodological considerations. *Quaternary International*, 362:14–22, 2015.

J. O. Stone. Air pressure and cosmogenic isotope production. *Journal Of Geophysical Research*, 105:23753–23759, 2000.

K. J. Thomsen, A. S. Murray, M. Jain, and L. Bøtter-Jensen. Laboratory fading rates of various luminescence signals from feldspar-rich sediment extracts. *Radiation Measurements*, 43(9–10): 1474–1486, 2008.

S. M. Uppala, P. W. KÅllberg, A. J. Simmons, U. Andrae, V. D. C. Bechtold, M. Fiorino, J. K. Gibson, J. Haseler, A. Hernandez, G. A. Kelly, X. Li, K. Onogi, S. Saarinen, N. Sokka, R. P. Allan, E. Andersson, K. Arpe, M. A. Balmaseda, A. C. M. Beljaars, L. V. D. Berg, J. Bidlot, N. Bormann, S. Caires, F. Chevallier, A. Dethof, M. Dragosavac, M. Fisher, M. Fuentes, S. Hagemann, E. Hólm, B. J. Hoskins, L. Isaksen, P. A. E. M. Janssen, R. Jenne, A. P. Mcnally, J. F. Mahfouf, J. J. Morcrette, N. A. Rayner, R. W. Saunders, P. Simon, A. Sterl, K. E. Trenberth, A. Untch, D. Vasiljevic, P. Viterbo, and J. Woollen. The ERA-40 re-analysis. *Quarterly Journal of the Royal Meteorological Society*, 131(612):2961–3012, Oct. 2005.

A. G. Wintle and A. S. Murray. A review of quartz optically stimulated luminescence characteristics and their relevance in single-aliquot regeneration dating protocols. *Radiation Measurements*, 41: 369–391, 2006.

M. G. Wolman. A method of sampling coarse river-bed material. *Transactions, American Geophysical Union*, 35(6):951–956, 1954.